Chemical Science

ROYAL SOCIETY OF CHEMISTRY

REVIEW

View Article Online
View Journal | View Issue

Cite this: *Chem. Sci.*, 2026, **17**, 8345

Molecular engineering of metalloporphyrins and phthalocyanines for homogeneous and heterogeneous CO_2 electroreduction

Aakash Santra, †[a] Arnab Ghatak,†[a] Zhiyuan Chen,[b] Jing Shen,[c] Joost Helsen,[b] Yuvraj Birdja,[b] Ally Aukauloo *[a] and Chanjuan Zhang *[b]

Received 15th October 2025
Accepted 6th March 2026

DOI: 10.1039/d5sc07983g

rsc.li/chemical-science

This review provides an overview of recent advances in CO_2 electrocatalysis, starting with the development of homogeneous electrocatalytic systems. We focused on porphyrin and phthalocyanine based molecular catalysts where different chemical strategies have been implemented drawing inspiration from natural enzyme systems that process CO_2, such as hydrogen bonding, proton relay, bimetallic cooperative action, electrostatic interactions and structural dynamics to help enhancing the selectivity and efficiency of electrochemical CO_2 reduction. The discussion then expands to heterogeneous processes in traditional H-cells, and more relevant flow-cell setups integrated with gas diffusion electrodes. A special focus is given to the growing trend of hybrid molecular-metallic co-catalyst systems, which are driving significant progress in heterogeneous CO_2 electrocatalysis.

1 Introduction

The electrochemical reduction of CO_2 to small molecular products (*e.g.*, CO, formate, methanol, ethylene, ethanol, acetate) is a promising route for sustainable fuel and chemical production while mitigating CO_2 emissions. Recent advances in catalyst design,[1] process optimization,[2] and electrolyzer engineering[3] have significantly improved selectivity, activity and stability.

Scientists have developed various catalysts for CO_2 electrocatalysis, with material selection depending on the target product, silver-based catalysts,[4] metalloporphyrins,[5] and metallo phthalocyanines[6] show high selectivity (>90%) for CO production, while Sn and Bi catalysts achieve >90% formate selectivity,[7] and molybdenum carbide and cobalt phthalocyanines excel in methanol generation.[8,9] Copper-based catalysts dominate methane production. Moreover, for C_{2+} products like ethanol and ethylene, copper remains the primary catalyst enabling C–C coupling, often *via* CO intermediates. To enhance C_{2+} selectivity, bimetallic catalysts such as AgCu have been explored, leveraging Ag's role in CO formation and Cu's ability to promote C–C coupling.[10] Recently, co-catalyst systems combining molecular catalysts with copper metallic catalysts for CO_2-to-C_{2+} conversion have emerged, demonstrating promising potential in the field.[11] An excellent catalyst is crucial for efficient CO_2 electrocatalysis to value-added chemicals, but process engineering and system integration are equally vital for industrial scalability. Extensive research has focused on optimizing C_{2+} selectivity through electrolyte engineering, with alkaline electrolytes suppressing hydrogen evolution but suffering from carbonate precipitation, which reduces electrolyzer longevity. Conversely, neutral electrolytes with additives like Cs^+ can stabilize *CO intermediates, boosting C_{2+} yields.[12] Other critical factors include CO_2 solubility (affecting reaction kinetics), operational temperature (influencing mass transport and reaction rates), and advanced materials like anion-exchange membranes (AEMs) that enhance CO_2 transport while minimizing crossover. Additionally, hydrophobic gas diffusion electrodes (GDEs) prevent flooding and improve triple-phase boundaries, further optimizing CO_2 reduction efficiency.

Dioxycle startup[13] exemplifies both the immense potential and the significant hurdles within the CO_2 electrolysis sector. The company's core technology aims to convert captured CO_2 into valuable ethylene and other chemicals, positioning it at the forefront of the carbon-to-value economy. However, its path to commercialization is currently constrained by a fundamental scientific challenge: the absence of a catalyst that is simultaneously highly active, selective, and durable over extended periods. The catalyst instability is the primary bottleneck preventing reliable performance at scale, similar to the pre-funded European Horizon projects like ICO_2NIC and SELECTCO2.[14,15] Without a robust catalyst that can maintain efficiency under

[a]*Université Paris-Saclay, Institut de Chimie Moléculaire et des Matériaux d'Orsay, UMR 8182 CNRS, 91400, Orsay, France. E-mail: ally.aukauloo@universite-paris-saclay.fr*

[b]*Electrochemical Excellent Center, Flemish Institute for Technological Research (VITO), Boeretang 200, 2400 Mol, Belgium. E-mail: chanjuan.zhang@vito.be*

[c]*Department of Chemistry, College of Chemistry and Chemical Engineering, Hunan Institute of Engineering, Xiangtan 411104, Hunan, China*

† A. S. and A. G. contributed equally to the work.

industrial operating conditions, such as high current densities and impure gas feeds, scaling up from lab-scale prototypes to megawatt-scale electrolyzers become economically and technically unviable. Consequently, while Dioxycle's system design and engineering are innovative, the unresolved catalyst issue remains the critical barrier to achieving further investment, successful pilot demonstrations, and ultimately, industrialization.

Therefore, the development of highly active, selective and durable electrocatalysts is the critical pathway to unlocking the economic viability and scalability of CO_2 electrolysis value chain. To be considered a viable candidate for industrial CO_2 electrocatalysis, a catalyst at the lab scale should meet the following key metrics: a current density exceeding 0.2 A cm^{-2}, a faradaic efficiency (FE) for C-products greater than 80%, and operation at a cell voltage under 3.0 V, with voltages below 2.0 V being ideal. Molecular catalysts, particularly bio-inspired metalloporphyrins and metallophthalocyanines, have emerged as highly promising materials for carbon dioxide reduction reaction (CO_2RR) due to their remarkable activity and tunability. This review summarizes the recent development, starting with advancements in homogeneous catalytic systems. We then extend the discussion to heterogeneous processes in conventional H-cells, progress to the more technologically relevant flow-cell configuration and conclude with perspectives on the molecular design requirements for industrial-scale CO_2 electroreduction.

Drawing inspiration from the functioning of natural enzyme systems dealing with the chemistry of CO_2, researchers have developed numerous bio-inspired molecular catalysts for CO_2RR and reviewed in recent literature. This review systematically explores the development of bio-inspired molecular catalysts for CO_2 electrocatalysis, charting their progression from homogeneous systems to heterogeneous H-cell configurations. We also examine their application at the laboratory scale in flow cell setups, with particular emphasis on integration with gas diffusion electrodes. Special attention is given to the emerging trend of hybrid molecular-metallic co-catalyst systems, a promising innovation driving advancements in heterogeneous CO_2 electrocatalysis.

2 Bio-inspired molecular catalysts for homogeneous CO_2 electrocatalysis

Among contemporary CO_2 conversion strategies, molecular catalysts stand out as a particularly promising avenue. Their tunable structures enable precise control over reactivity, allowing iterative modifications to introduce functional groups that improve selectivity in CO_2 transformation.[16,17] Over the past decades, significant research efforts have been devoted to developing efficient metal-based molecular catalysts within the frameworks of classical coordination and organometallic chemistry. Another strategic approach employed by bioinorganic chemists to develop cost-effective molecular catalysts involves mimicking the structural features of enzyme active sites involved in CO_2 conversion, such as Carbon Monoxide Dehydrogenase (CODH). Insights have also been drawn from other enzymatic systems like cytochrome *c* oxidase, which catalyzes the reduction of O_2 to H_2O, to inform the design of novel molecular architectures for CO_2 reduction. For example, since the 1980s, iron tetraphenylporphyrins (FeTPP, **1**, Fig. 1a) have been recognized as highly effective catalysts for the homogeneous electroreduction of CO_2 to CO in organic solvents. Building on this discovery, FeTPP has served as a foundational molecular platform for incorporating key functional and structural motifs inspired by enzymatic active sites. These modifications are designed to improve catalytic performance, selectivity, and stability in CO_2RR. This strategy has already enabled significant breakthroughs and it continues to pave the way for new discoveries in the field.[18] Setting aside the critical role of the entire protein matrix in metalloenzyme function, which remains beyond the reach of current chemical modeling (Fig. 1b), chemists aim to harness nature's most efficient catalysts by focusing on a few fundamental principles, namely:

(i) Hydrogen bonding.
(ii) Confined water molecules.
(iii) Bimetallic cooperativity.
(iv) Local proton source.
(v) Electrostatic interactions.
(vi) Entatic states.
(vii) Structural dynamics.

In the sections that follow, we summarize key findings related to the incorporation of each of these functional elements into the periphery of molecular-based CO_2 reduction catalysts.

2.1 Hydrogen bonding

Hydrogen bonding interactions are widely recognized as one of the key factors contributing to the remarkable efficiency and selectivity of metalloenzymes. For instance, at the active site of CODH, hydrogen bonding from a lysine and a histidine help to stabilize CO_2 adducts and transition states, lowering the energy barriers associated with multi-electron, multi-proton transformations. This stabilization is often highly directional and localized, allowing the enzyme active site to precisely control the reaction pathway and favor specific products over undesired side reactions. While this strategy has been elegantly developed for O_2 activation and reduction.[19–21] Dey and co-workers used it in CO_2RR and made significant contributions incorporating intramolecular hydrogen bonding (H-bonding) from pendant

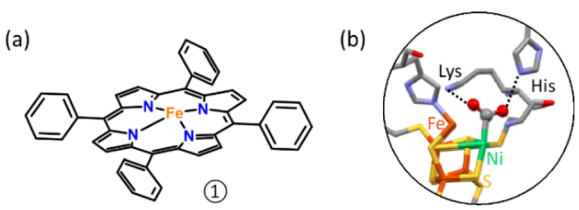

Fig. 1 (a) Chemical structure of iron tetraphenylporphyrin (FeTPP, **1**), (b) active site of CO dehydrogenase showing heterobimetallic [NiFe] and hydrogen bonding [Lys, His] activation of CO_2.

second sphere moieties over simple mononuclear porphyrins, that changed both reactivity as well as selectivity of CO_2RR. The authors associated hydrogen bond donor groups with both hydrophobic and hydrophilic groups and investigate their effects by synthesizing catalyst **2**, **3** and **4** (Fig. 2).[22] Catalyst **2** holds an amide function together with a pivaloyl group providing a hydrophobic environment. In contrast catalyst **3** and catalyst **4** contain a hydrophilic environment in the immediate vicinity of the catalytic center provided by the four triazoles in the distal pocket known to contain H_2O molecules entrapped into the cavity. Under homogeneous electrochemical conditions in CH_3CN, all the complexes showed catalytic current for CO_2 reduction from their respective $Fe^{I/0}$ potentials which were very close to each other, in presence of 3 M phenol. The product for CO_2RR was analyzed to be mainly CO and foot of the wave analysis (FOWA) revealed the relative catalytic rate for catalyst **4**, **3** and **2** were 2.5×10^2 s^{-1}, 1×10^3 s^{-1}, and 5.1×10^5 s^{-1}, respectively, demonstrating the fact that TOFs vary by an unprecedented range of $\sim 10^3$. Supported by DFT analysis, the authors proposed a catalytic cycle in which CO_2 activation by the Fe^0 species is facilitated by the positive amide dipole positioned near the active iron site in catalyst **2**. This interaction aids in stabilizing the bound CO_2 intermediate; however, this step was not identified as the rate-determining step (RDS). Instead, the RDS was determined to be the protonation of the C–OH moiety in the Fe^{II}–COOH intermediate, particularly in the presence of an external proton donor, as this protonation step is essential for C–O bond cleavage. The enhanced performance of catalyst **2** was attributed to the presence of a pre-organized hydrogen-bond donor group, which effectively assists in the O-protonation step and facilitates the subsequent release of the CO product. In contrast, catalysts **3** and **4**, which lack such pre-organized H-bond donors, rely on a trapped H_2O molecule that functions as a hydrogen-bond acceptor. This configuration does not contribute meaningfully to CO_2 activation or efficient C–O bond cleavage, thereby leading to reduced catalytic activity compared to catalyst **2**.

With similar approach, Chang and co-workers, synthesized 4-sets of positional isomers, where they put second sphere proximal and distal amide moieties in the *ortho* positions of *meso*-aryl group and in the corresponding *para* positions over a simple mono nuclear iron porphyrins to find the role of H-bond donor effect from different positions through space.[23] Among the four catalysts of, **5**, **6**, **7** and **8** (Fig. 2), the *ortho* one with distal amine group (2-position, **6**) was found to be most efficient electrocatalyst for CO_2RR with log TOF_{max} value of 6.74 at −2.18 V *vs.* Fc^+/Fc with corresponding k_{cat} value of 3.33×10^8 M^{-2} s^{-1}, which exceeded other systems by 2-orders in magnitude in both TOF and k_{cat} value. The FE of 92% for CO formation as a product was also obtained for **6**, which was the highest for these sets of catalysts. They further showed CO_2 binding constant (determined based on the potential shift of the formal $Fe^{I/0}$ couple under Ar and CO_2) for the *para* substituted amides were very low from 2–4 M^{-1}, comparable with that of **1**, while for the *ortho* amides the affinity was high ∼14–17 M^{-1}. This indicated that proper positioning of the amide functions is critical to establishing suitable hydrogen bonding interactions with the metal carboxylate intermediate and the second sphere hydrogen bond donors must be placed at *ortho* positions of the porphyrin scaffolds. In between the two *ortho* isomers, distal amide one showed most effective breaking of the electronic scaling relationship for CO_2 reduction due to enhanced hydrogen bond stabilization of the Fe–CO_2 intermediate.

Dey and co-workers further investigated the role of H-bond donors in the mechanistic pathways. When the log of catalytic rate of CO_2 reduction was plotted as a function of pK_a of different H-bond donor groups (like catechol, *ortho*-2-amide, picket fence-amide and triazole moieties),[24,25] a linear dependence with a slope of 0.29 was obtained. This implied two things – (a) even with same external acid source the pK_a of the H-bonding donor group controls the rate of CO_2RR as rate of electrocatalytic reduction was determined to be a concerted reduction, protonation and C–OH bond cleavage of intermediate Fe^{II}–COOH, (b) substantial involvement of proton transfer in RDS and hence a k_H/k_D value of 3.28 was obtained, when external acid source of PhOH was replaced by PhOD. Under these circumstances, a general mechanism was proposed, with iron porphyrins having distal H-bonding residues (Fig. 3). After the formation of Fe^{II}–COOH species, the O-protonation to release CO could not be achieved by weak external acid like

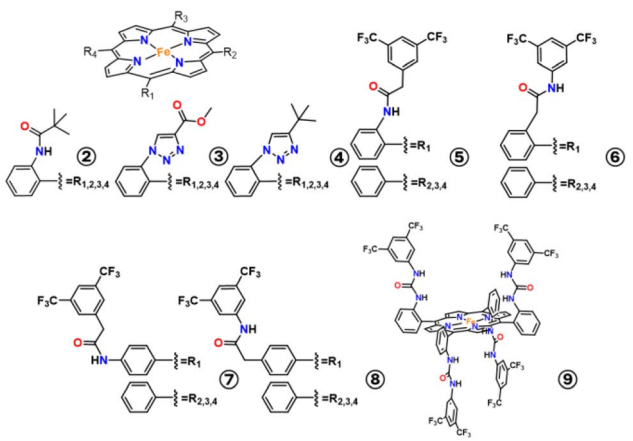

Fig. 2 Chemical structures of iron porphyrins with distal second sphere hydrogen bonding residues, discussed in the review.

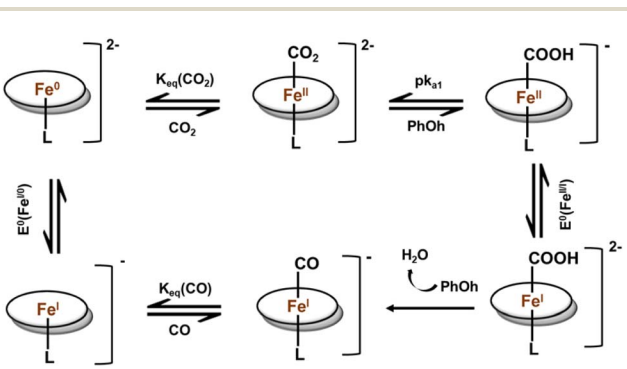

Fig. 3 Schematic representation of the proposed mechanism by iron porphyrin with second sphere distal hydrogen bonding residues under electrochemical condition with mild acid.[22]

PhOH and it would be hydrolysed to form HCOOH. Thus, most plausible pathway would be reduction of Fe^{II}–COOH to Fe^{I}–COOH under the electrochemical condition and then protonation of the Fe^{I}–COOH species to cleave the C–OH bonds, which is likely the RDS in these electrochemical reduction reactions under conditions where the overpotential (η) is large enough for the electron transfer to be faster than the chemical steps (Fig. 3). This is also consistent with the dependence of the catalytic rate on the pK_a of the hydrogen bonding residues. This particular role of H-bond in tuning the CO_2 reduction rate is also reflected in the catalytic Tafel plot, proposed by Savéant *et al.*[26]

The effect of second sphere hydrogen bonding over iron porphyrins also altered the electroactive state of Fe by decreasing the catalytic overpotential for CO_2RR, as has been shown by our group.[27] In their early attempts to mimic the lys_{563} and His_{93} residues present in the second sphere of enzyme CODH, Aukauloo and co-workers first envisioned a superstructured iron porphyrin with four urea functionalities modified with electron withdrawing –CF_3 moieties (**9**, Fig. 2).[28] In the crystal structure of **1b**, presence of entrapped water molecules in the vicinity of the urea functions was also notified. A large thermodynamic advantage (over 300 mV anodic shift in η) in the catalytic CO_2 reduction under CO_2 saturated organic solvent using water as proton source, was obtained for catalyst **9**, compared to simple **1**. Despite that, breaking the scaling relationship as discussed by Costentin and Savéant,[5] the efficiency of catalyst **9** for CO_2RR to CO in terms of TOF remained same as compared to **1**. Initial electrochemical results in absence of proton source indicated towards an order of higher magnitude of CO_2 binding constant for **9** compared to that for control **1**. But, the theoretical calculation from DFT optimized CO_2-bound Fe^0-**9** compound showed two strong hydrogen bonds were engaged by each urea arms of **9** yielding four short N(H)···O distances of 2.738, 2.804, 2 × 2.832 Å, which is comparable to the native CODH enzyme as well and due to this multipoint H-bonding a 29 kcal mol^{-1} stabilization on CO_2 anchoring was achieved by catalyst **9**. As shown by Gotico *et al.*[28] in presence of external water as a source of proton for catalysis, this multipoint hydrogen bonding got strengthened through water network mediation, which was a sharp contrast to another recent study in thiourea-tethered rhenium catalyst by Neumann and co-workers.[28] Under homogeneous electrochemical condition with H_2O as proton source **9** was able to reduce CO_2 to CO with k_{cat} 2.76 × 10^3 s^{-1} and log TOF_{max} 3.83, comparable with **1** even with 300 mV gain in η.

As discussed earlier, using the multipoint hydrogen bonding effect present in **9**, Amanullah *et al.* was able to activate the Fe^{I} species instead of Fe^0 species for CO_2RR and got CO as the major product.[27] *In situ* FTIR-SEC experimental data during a controlled potential electrolysis (CPE) at −1.55 V *vs.* Fc^+/Fc in DMF solution showed the formation of C=O band of Fe^{II}–CO species denoted by 1958 cm^{-1}, but at that potential no catalytic CO was detected. Catalytic CO formation *via* Fe^{II}–CO species was found at −1.65 V potential and both these potentials were negative enough to generate the Fe^{I} but not reaching the potential to generate Fe^0, which was −1.79 V. They methodically through single turnover experiments at low temperature were able to trap the intermediate Fe^{III}–CO_2^-, followed by the formation of Fe^{III}–CO_2H and ultimately reaching to Fe^{II}–CO, and characterized them with UV-vis, EPR, IR and rR spectroscopy, and mechanism of CO_2RR by **9** was established from its formal Fe^{I} state. At −1.55 V, $UrFe^{III}$ was reduced *via* two electrons to Fe^{I}, which was the active species for CO_2 capture and starting the reduction (Fig. 4). The urea group from second sphere came into the scenario at that state first for CO_2 capture and then aiding in formation of ferric LS $[Fe^{III}–CO_2]^-$ species with *g*-values of 2.29, 2.17 and 1.95 (from EPR), along with rR marker bands at ν_4 = 1368 cm^{-1}, ν_2 = 1568 cm^{-1} and λ_{max} = 440 nm (Fig. 4). The next step was the protonation in presence of trace amount of water to form HS Fe^{III}–CO_2H species with *g*-values of 5.99, and 1.99 (from X band EPR), along with rR marker bands at ν_4 = 1360 cm^{-1}, ν_2 = 1553 cm^{-1} and λ_{max} = 430 nm. The corresponding ν(Fe–C) = 588 cm^{-1} and ν(C–OH) = 1208 cm^{-1} were detected from rR as well. In the following step, Fe^{III}–CO_2H was further reduced (E_0 = −1.05 V *vs.* Fc^+/Fc) to form the HS-Fe^{II}–CO_2^-, characterized by λ_{max} at 439 nm from UV-vis, with rR marker bands at ν_4 = 1347 cm^{-1}, ν_2 = 1545 cm^{-1}, ν(Fe–C) = 436 cm^{-1}, ν(C–OH) = 1109 cm^{-1} and infrared frequency at ν(C=O) = 1679 cm^{-1} (Fig. 4). A last proton transfer was induced to release water molecule and ensured the formation of Fe^{II}–CO, from where catalytic formation of CO was detected (Fig. 4). The source of the proton for this step could come from a water molecule or a bicarbonate trapped in the urea arms present in the second sphere of the catalyst.

Hydrogen bonding interactions play a crucial role in enhancing the efficiency and selectivity of metalloenzymes and synthetic catalysts for CO_2 reduction, with specific donor groups and their positioning significantly affecting catalytic rates and product selectivity. Studies show that catalysts with pre-organized hydrogen-bond donors, such as amide groups in certain positions, outperform those relying on water molecules as hydrogen-bond acceptors, due to better stabilization of

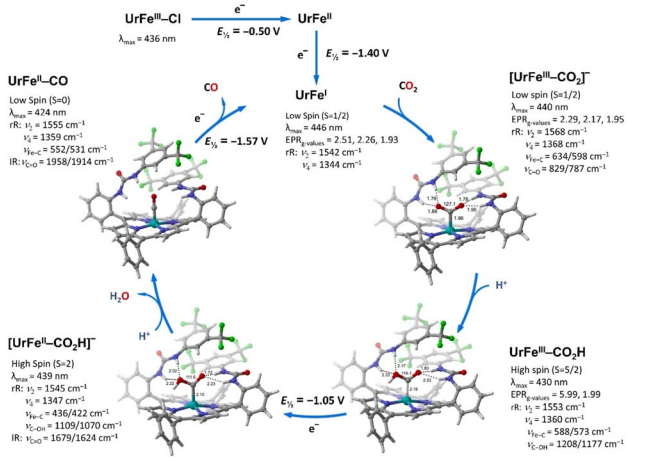

Fig. 4 Schematic representation of the proposed mechanism for **9** during electrocatalytic CO_2RR at a potential less negative than that needed to reach Fe^0 state, as shown by Aukauloo and co-workers. Reproduced with permission from ref. 6 and 27. Copyright 2023 John Wiley and Sons.

reaction intermediates and facilitation of key protonation steps. The catalytic rate is closely linked to the pK_a of the hydrogen-bond donor group, and multipoint hydrogen bonding can lower overpotentials and stabilize CO_2 binding, further improving catalytic performance. A comprehensive summary of the performance of all the catalysts discussed in this section is shown in Table 1.

2.2 Confined water molecules

Water mediated hydrogen bonding in presence of hydrogen bond acceptor residues plays important role in CO_2RR product selectivity.

Placing one basic distal pyridine group in the second sphere of iron porphyrin (**10**, Fig. 5) Dey and co-workers were able to take advantage of intra molecular hydrogen bonding in their subsequent work to stabilize the metal bound CO species, enabling multielectron multiproton CO_2RR.[29] They showed catalyst **10** was electroactive in CO saturated CH_3CN environment and due to the presence of basic distal pyridine residue was able to reduce CO to CH_4 with 93% FE, with a given proton source. Spectro-electrochemistry coupled FTIR (FTIR-SEC) was employed to understand the mechanism of the reaction with its *in situ* identification of the metal carbonyl species, using isotope sensitive absorption. In CO saturated CH_3CN solution of catalyst **10** containing 3% H_2O they identified Fe^{II}–CO species being reduced to Fe^{I}–CO at −1.75 V potential, followed by the reduction of Fe^{I}–CO to Fe^{0}–CO at −2.35 V *vs.* Fc^+/Fc. Captivating was the fact that holding the potential at −2.35 V for a longer period of time a new adduct Fe^{II}–CHO was generated which could be further reduced to CH_4. Basically, pyridine mediated hydrogen-bonding between water molecules (*i.e.*, proton source) and Fe^{I}–CO intermediate allowed its required stabilization for the further activation reduction to CH_4 (as evidenced by DFT calculation).

In their continued effort, Dey group demonstrated within the same molecular framework of mononuclear iron porphyrin, inclusion of systematically stronger hydrogen bonding groups changed the product selectivity of CO_2RR.[30] Over FeTPP molecule, they incorporated 1,10-phenanthroline moieties in the second sphere to prepare catalyst **11** (FeMonophen) and **12** (FeBisphen) (Fig. 5) respectively. Notably, in CO_2 saturated CH_3CN solution in presence of 5% H_2O, at −2.3 V *vs.* Fc^+/Fc the

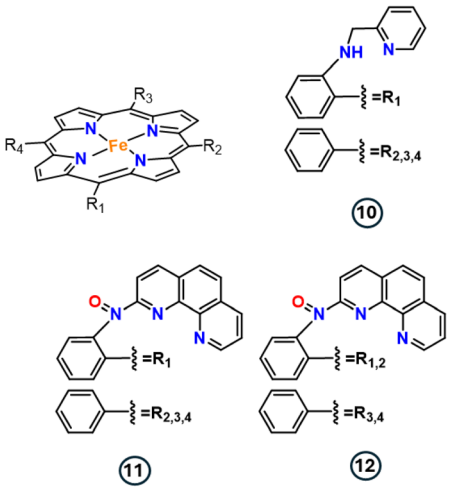

Fig. 5 Chemical structures of iron porphyrins with confined water molecules.

major product was 76% HCOOH for catalyst **12**, while 53% CO as major product for catalyst **1** (without HCOOH) and a mixture of 34% HCOOH and 23% CO for **11** was obtained in terms of FE (Fig. 6A). After detecting Fe^0 to be the electroactive state, Patra *et al.*[30] chemically reduced Fe^{II} porphyrins to the formal Fe^0 state, before bubbling CO_2 gas at −80 °C to chemically trap the Fe^{II}–COOH species through resonance Raman spectroscopy. Raman spectroscopic data indicated (from ν_4 and ν_2 sets of marker bands) the formation of exclusively low spin (LS)-Fe^{II} species for **1**, while due to the presence of the intra molecular H-bonding for Fe-monophen (**11**) a mixture of LS and high spin (HS) Fe^{II} and for **12** exclusively HS-Fe^{II} species were obtained. FTIR-SEC *operando* data for **12** at −2.3 V indicated the rise of a ν(C=O) peak at 1639 cm^{-1} (Fe^{II}–COOH), which was found to be rather weaker at 1620 cm^{-1} for **1**. Inclusion of H-bonding group allowed the shift in spin state of the Fe^{II}–COOH intermediate from LS to HS, resulting in stronger C=O stretch corresponding to weaker back bonding from HS Fe^{II}. Finally, DFT calculation showed Fe–C bond was substantially more covalent in the low spin state due to stronger σ bonding between the Fe^{II} and –COOH. In general, LS Fe^{II} state exists for Fe^{II}–COOH species, where due to above reason the

Table 1 Comparison of the electrocatalytic CO_2RR performance of Fe porphyrins bearing hydrogen-bonding units

Catalyst	Electrolyte solution	E^0_{cat}/(V *vs.* NHE), η (V)	% FE (CO)	k_{cat}/k_{obs}	log TOF_{max}	Ref.
2	MeCN, 3 M PhOH	−1.27, 0.62	—	5.0×10^6 s^{-1}	5.70	22
3	MeCN, 3 M PhOH	−1.19, 0.54	—	1.0×10^3 s^{-1}	3.00	22
4	MeCN, 3 M PhOH	−1.15, 0.50	—	2.5×10^2 s^{-1}	2.39	23
5	DMF, 0.5 M PhOH	−2.12[a], 0.95	83	1.01×10^6 M^{-2} s^{-1}	4.35	23
6	DMF, 0.5 M PhOH	−2.18[a], 1.00	92	3.33×10^8 M^{-2} s^{-1}	6.74	23
7	DMF, 0.5 M PhOH	−2.15[a], 1.05	74	1.03×10^4 M^{-2} s^{-1}	2.23	23
8	DMF, 0.5 M PhOH	−2.16[a], 1.05	79	4.20×10^5 M^{-2} s^{-1}	3.84	12
9	DMF, 5.5 M H_2O	−1.12, 0.63	91	2.76×10^3 s^{-1}	3.83	28

[a] For these systems the potentials are reported *vs.* Fc^+/Fc electrode and data were collected using secondary reference electrode.

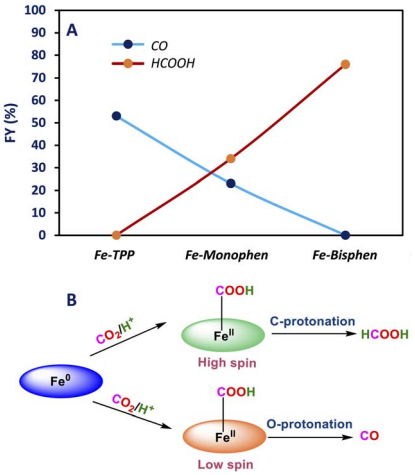

Fig. 6 FE (%) of both CO (blue trace) and HCOOH (red trace) for catalysts **1**, **11** and **12** respectively (A). Schematic representation of the CO_2RR mechanism based-on the spin state of the Fe^{II}–COOH intermediate, as shown by Dey and co-workers (B). With permission from ref. 27 and 30. Copyright 2025 Elsevier.

electron density of the C-center was depleted and O-protonation in the successive state became more favorable resulting in the formation of CO, for **1** (Fig. 6B). Only when, strategic hydrogen bonding was installed, the ground state Fe^{II}–COOH species became a high spin one due to phenanthroline moieties in the second coordination sphere weakening the Fe–C bond, which favored carbon atom protonation and subsequent formation of HCOOH instead of CO (Fig. 6B).

Although, these set of examples of water mediated hydrogen bonding help immensely in tuning the product selectivity, still entails a paradox about the pK_a of the confined water molecule. The pK_a of this channeled water should be different from the bulk water and that should be kept in mind while designing future catalysts.

In brief, water-mediated hydrogen bonding with strategically placing hydrogen bond acceptor groups in iron porphyrin catalysts can significantly influence the product selectivity CO_2RR enabling the conversion of CO to CH_4 and shifting selectivity between CO and HCOOH depending on the catalyst design. It highlights the role of spin state changes in Fe^{II}–COOH intermediates, showing that stronger hydrogen bonding groups in the catalyst's second sphere can favour the formation of HCOOH over CO by altering the electronic structure and protonation pathways. This also signifies the importance of considering the altered pK_a of confined water molecules in catalyst channels for future catalyst design.

2.3 Bimetallic cooperativity

The presence of multinuclear active sites is a common feature in many substrate-activating enzymes. In the case of [NiFe]-CODH, for example, a redox-active nickel ion works synergistically with an iron(II) center that functions as a Lewis acid. This arrangement exemplifies a division of labor strategy, in which one metal ion (nickel) is capable of cycling through multiple oxidation states, making it well-suited for electron transfer and redox reactions. Meanwhile, the Lewis acidic iron(II) ion plays a complementary role by stabilizing negative charges that develop on the substrate or transition states during catalysis. It can also activate water molecules, thereby facilitate nucleophilic attack and enhance the overall redox process. This cooperative interaction between distinct metal centers enables the enzyme to carry out complex chemical transformations with remarkable efficiency and specificity. Saveant and co-workers way back in 1991, paved the pathway for bimetallic cooperativity for CO_2RR.[31] In this study, they used the parent FeTPP (**1**), together with other porphyrins with secondary amide groups as the catalysts. They found that, although Fe^0 was the active state for catalysts for CO_2RR with CO being the major product at −1.8 V *vs.* SCE, after small number of cycles in electrochemistry the porphyrin ring rapidly degraded due to carboxylation/hydrogenation. When, Saveant *et al.* added Mg^{2+} in the electrolysis solution as a non-hydrated salt with weakly nucleophilic counter anion, a rise in catalytic activity and CO selectivity (as product) was achieved. At low temperature of −40 °C the catalytic efficiency was further increased. At low temperature as well as at room temperature (20 °C), the catalytic process began with the introduction of one molecule of CO_2 in the coordination sphere of the iron atom, forming a carbene-type complex in which electrons were transferred from the iron porphyrin to the CO_2 moiety. At low temperature, the second step, in the absence as well as in the presence of Mg^{2+} ions, was the addition of a second molecule of CO_2 in an acid–base-type manner. The C–O bond of the first CO_2 molecule was then broken with formation of the Fe^{II}–CO complex and of a carbonate ion. This reaction was accelerated by the presence of Mg^{2+} ions, presumably through the intermediary formation of a magnesium complex. At room temperature, the Mg^{2+} ions participate earlier to the breaking of the C–O, namely at the level of the first iron–CO_2 adduct. Mg^{2+} ion acted as an electron-poor centre, facilitating the bond transformation similar to electrophilic assistance in nucleophilic substitution initiated by the electron-rich Fe^0 centre. However, Mg^{2+} ions functioned as a co-substrate rather than a cocatalyst.

A simplistic approach to interrogate the concerted action of two metal centers for the CO_2RR was proposed by the group of Yamamoto back in 2003, where the authors rely on the formation of metalloporphyrin dimers by mixing a cationic tetrakis(*N*-methylpyridil) porphyrin (TMPyP) and an anionic tetra(4-sulfonatophenyl) porphyrin (TPPS) in solution to form Co–Co dimers (catalyst **13**, Fig. 7).[32] The formation of dimers was confirmed by the drastic decrease in Soret band of UV-visibile spectra in solution, attributed to π-stacking in a cofacial manner. CV data of the dinuclear **13** complex in DMSO under Ar atmosphere showed more reversible Co redox peaks compared to mononuclear Co-TMPyP, especially for the $Co^{II/I}$ couple at −1.8 V *vs.* Ag/Ag^+. This was attributed to the fact that axial coordination of the solvent molecule was inhibited after dimerization, although less dynamic exchange of ligands could be the reason. Co^I-TMPyP acted as the active catalyst (confirmed by Yamamoto *et al.*[32] coinciding with the position of the catalytic peak using rotating disk voltammetry) for CO_2RR in DMSO,

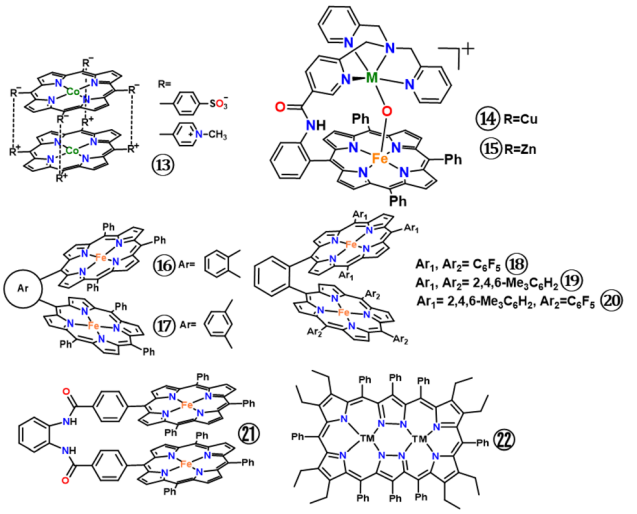

Fig. 7 Chemical structures of porphyrin-based bimetallic catalysts discussed in the review.

with CO and formate being the major product, where the role of CoTPPS was an electron mediator. But they didn't clarify the redox activity of CoTPPS after the dimerization. Nonetheless, due to dimerization the activity was found to be twice than that of mononuclear ones, in terms of kinetic current density. Yamamoto and co-workers also tried with other metalated TPPS moiety, getting less or almost similar reactivity showcasing a new concept altogether for bimetallic porphyrin catalyst design.

From these examples of bimetallic cooperativity between independent molecular systems, chemists went on to design molecular scaffolds that can hold both metal ions in a controlled topology. For instance, Zhang and co-workers designed an iron porphyrin decorated with a pyridine based ligand (tris(pyridine-2-ylmethyl) amine, (TPA)) for the facile inclusion of a second metal ion (Zn^{2+} and Cu^{2+}) to form the bimetallic catalysts FeCu (**14**) and FeZn (**15**) respectively (Fig. 7).[33] Supported by DFT calculation, they showed that the distal metal ion was connected to the iron porphyrin center *via* an oxo bridge. The CV response in DMF solution, showed the synergistic effect of secondary sphere metal ions, when the $Fe^{I/0}$ redox couple was slightly shifted anodically by 40 mV for FeCu **14** (from CuTPA) and by 190 mV for FeZn **15** (from ZnTPA) respectively. In presence of CO_2 and phenol as proton source, both **14** and **15** exhibited higher catalytic activity from the $Fe^{I/0}$ state compared to the mononuclear counterparts, at low onset potential. Corresponding FOWA analysis for the CO_2RR revealed log TOF_{max} values of 7.43 (at −2.06 V *vs.* Fc^+/Fc) and 6.62 (at −1.91 V *vs.* Fc^+/Fc) for **14** and **15** respectively, which were higher than simple iron porphyrin having only 2.94 log TOF_{max} value at −2.10 V *vs.* Fc^+/Fc (almost two orders increase in TOF value). Also, when log TOF was varied as a function of η, **14** and **15**, outperformed simple mononuclear porphyrin **1**, producing higher TOF at low overpotential. Controlled potential electrolysis at −2.30 V *vs.* Fc^+/Fc for 3 hours and the corresponding product analysis revealed CO as the major product of CO_2RR, for all these catalysts with turnover number (TON) for **14**, **15** and **1** were 61, 70 and 5.8 respectively. The outperformance of the bimetallic catalysts in the kinetics as well as product selectivity emphasized the role of distal metal ion in CO_2RR. Through redox titration of **15** with KC_8 and monitoring with UV-visible spectroscopy they provided a mechanism for this bimetallic activity for CO_2RR by catalyst **15**. At first, $1e^-$ reduction of the initial species, produced $[Fe^{II}TPPZn^{II}]^{2+}$ intermediate with μ-oxo loss. Subsequent $2e^-$ reduction yielded the major intermediate species $[Fe^{I}TPP\text{-}Zn^{II}]^0$. This active species underwent reductive CO_2 binding by Fe^I to form $[FeTPP(CO_2)Zn]^0$. At this stage, distal Zn^{2+} coordinated to a O atom of CO_2 and subsequent protonation led to the formation of $[FeTPP(\text{-}COOH)Zn]^+$. Another protonation and followed by $2e^-$ reduction would regenerate $[Fe^{I}TPP\text{-}Zn^{II}]^0$ and CO would be released as the major product. This is how Zn^{2+} provided stability in CO releasing activity. Energy profile calculation from DFT indicated, when CO_2 binds to $[FeZn]^0$, 27.7 kcal mol^{-1} stability is obtained for the formation of $[Fe(CO_2)Zn]^0$ and this process occur without a transition state. This is unlike the energy profile for the monomer, where energy barrier of CO_2 binding is high and only 0.72 kcal mol^{-1} stability is obtained after CO_2 binding. This further proved the thermodynamic advantage of cooperative binding by Zn^{2+} ion.

Naruta and his group reported in 2015, cofacial porphyrin dimers as a suitable ligand holding two iron centers.[34,35] They have systematically measured the catalytic CO_2RR activity of the cofacial iron tetraphenyl porphyrin dimer (*o*-Fe_2DTPP, catalyst **16**, Fig. 7) in DMF/10% H_2O solution and compared the results with the monomer **1** along with the corresponding 1,3-phenylene bridged iron porphyrin *meta* dimer (*m*-Fe_2DTPP, catalyst **17**, Fig. 7). The *ortho* dimer under catalytic condition showed benchmarking result with 95% FE_{CO} formation with k_{cat} value of 2.15×10^5 s^{-1} and TOF of 4300 s^{-1} at relatively high ∼0.66 V overpotential, where the catalytic wave was appearing over the Fe^I–Fe^I/Fe^I–Fe^0 redox couple, indicating any one to be the active species. This bimetallic catalyst was shown to be much more effective compared to monomeric **1** where i_{cat}/i_p value for **16** was 200, while that for **1** was only 35. Moreover, compared to the *meta*-dimeric configuration, the *ortho*-configuration exhibited high catalytic activity, owing to suitable separation of the two metal irons with a 3.2–4.0 Å Fe–Fe distance. The appropriate separation of the two iron ions was credited with **16**'s great activity, selectivity, and stability. When the Fe^{II} species was electro-generated, as shown by the CVs, CO_2 bind to the iron centers inside the cavity, which was made easier by this structure. Neither **1** nor **17** showed this behavior. Furthermore, a local push–pull mechanism was provided by the presence of two Fe centers at an appropriate separation distance. One Fe center functioned as a Lewis base (Fe^0), pushing an electron pair to the coordinated CO_2 molecule, while the other Fe center (Fe^I) functioned as a Lewis acid, promoting C–O bond cleavage and the formation of CO.

Pursuing their effort, Naruta and co-workers introduced electron withdrawing as well as electron donating substituents in the phenyl ring of the bimetallic dimer with the mindset to modulate the overpotential η as well as the reactivity.[36] With

a series of bimetallic dimers, through structure electronic effect was evidenced when presence of electron withdrawing fluorine atoms in the phenyl ring (Fe_2DTPFPP, catalyst **18**, Fig. 7) lowered the catalytic overpotential to 0.56 V while maintaining a similar reaction rate constant. In case of the monomeric control, in spite of having electron withdrawing fluorine atoms the trade of between high log TOF value at lower overpotential was not evidenced, further demonstrating the synergistic effect of the two metals. On the contrary, inclusion of electron donating groups (6 mesityl groups in Fe_2DTMP, catalyst **19**, Fig. 7) resulted in higher catalytic activity with TOF of 6×10^5 s^{-1}, but at high value of η of 0.91 V. With the heterodimer Fe_2TPFPP-TMP (catalyst **20**, Fig. 7) that had quite different electronic environment around the two Fe centers, they showed stepwise reduction of Fe centers under Ar, and catalytic wave was found over [$Fe^{I}Fe^{0}$] species. This further reinforced the fact that Fe^0 and Fe^{I} possibly act as a redox active site and the Lewis acid, respectively, in the catalysis process. Given that the Lewis acid should maintain its Fe^{I} state during/after the catalytic cycle, it is difficult to distinguish the attributed Lewis acid role from this CV measurement alone.

Continuing their effort to develop cofacial porphyrin dimers the same group has synthesized a new cofacial Fe-porphyrin dimer with a flexible *o*-phenylene amide bridge (f-Fe_2PD, catalyst **21**, Fig. 7) for electrocatalytic CO_2RR to CO.[37] **21** showed enhanced improvement for the CO_2-to-CO conversion starting at only $\eta = 0.15$ V which is the lowest reported overpotential in a homogeneous CO_2-saturated DMF/10% H_2O/1.0 M PhOH solution. In fact, this flexible dimer showed higher catalytic activity having TOF $= 2 \times 10^7$ s^{-1}, compared to that of the rigid dimer catalyst **16** with TOF $= 6 \times 10^2$ s^{-1} as well as the monomer with electron withdrawing fluorine atom (TOF $= 2 \times 10^3$ s^{-1}). The starting onset potential was −0.9 V *vs.* NHE only for **21**. The two amide groups with electron withdrawing inductive effect in the f-Fe2PD promoted the electro generation of the $Fe^{I}Fe^{0}$PD active species at more positive applied potential (−0.89 V) compared to that generated in the case of r-Fe2DP (−1.18 V). Along with this, two local protons in the two amide groups were anticipated to increase the catalytic activity by facilitating simple access for CO_2 to enter the porphyrin cavities and maximizing the local push–pull action between the two Fe centres. The flexibility of the bridge assuming various orientations on the polarized electrode enables this high reactivity. Although, there is no spectroscopic support or DFT optimized calculations shown by the authors regarding this. However, when **21** was integrated into ketjen black carbon surface (KBC) nanoparticles and grafted on the GC surface, under heterogeneous conditions of 0.5 M $NaHCO_3$ solution, it showed selective CO production in with current densities of 3.1–12.8 mA cm^{-2} at overpotentials of 0.26–0.46 V. The authors argued that their catalysts were stable enough over the electrode to exploit new CO_2 conversion technology.

With the same idea to make two metal centers to function together for the CO_2RR, Franc Meyer and co-workers reported an expanded porphyrin consisting of two pyrazole rings (abbreviated as the CTP ligand) that bridged two porphyrins like N4 coordination sites.[38] Building on this ligand coordination scheme Du and co-workers prepared a series of homo and heterobimetallic compounds to investigate their electrocatalytic activity towards CO reduction. In this work, backed by DFT calculations they have shown, that homobimetallic Co_2CTP (catalyst **22**, Fig. 7), and the corresponding heterobimetallic CoNiCTP enhance the adsorption of CO molecules through appreciable charge transfer from the metal ions.[39] As a consequence, chances of coupling of two adsorbed CO molecules increased and both these complexes showed high activity and selectivity towards conversion of CO to ethanol with a limiting potential (denoted as U_L can be obtained using the equation as $U_L = -\Delta G_{max}/e$, where ΔG_{max} the largest free energy change among the hydrogenation steps of the CO_2 reduction pathway) of only −0.59 V and −0.61 V (calculated from DFT) for Co_2CTP and CoNiCTP respectively. Theoretical calculations further indicated narrow band gap and shallower d band center could be attributed as the potential cause for the enhanced activity of Co bimetallic complexes with CTP ligands. Here, CO–CO dimerization was the potential determining step, showing the high free energy change in the whole CO reduction pathway. Such an approach and findings allowed the authors to propose that such bimetallic Co-based complexes as potential electrocatalyst for CO_2RR to C_2 products with high selectivity, which otherwise are very difficult to produce.

Presence of multinuclear active sites, particularly in synthetic catalysts, enable efficient and selective chemical transformations by leveraging the cooperative roles of different metal ions—such as nickel and iron in the native [NiFe]-CODH enzyme. Combinations like Fe/Mg or Co/Co in porphyrin-based system were shown to improve electron transfer, charge stabilization, and bond activation. Such studies reported above, indicated that introducing a second metal ion (*e.g.*, Mg^{2+}, Zn^{2+}, Cu^{2+}) or designing bimetallic complexes can dramatically enhance catalytic activity and selectivity for CO_2RR, often by stabilizing intermediates and lowering energy barriers. This section further illustrates how structural modifications—such as cofacial porphyrin dimers and flexible bridging ligands—optimize the spatial arrangement and electronic properties of metal centres, leading to superior performance in CO_2 conversion technologies. A comprehensive summary of the performance of all the catalysts discussed in this section is shown in Table 2.

2.4 Local proton source

Incorporating localized acidic proton sources near the periphery of CO_2RR catalysts has emerged as a pivotal strategy in recent catalyst design. This approach is inspired by enzymatic systems, where proton-coupled electron transfer (PCET) plays a central role in achieving high catalytic efficiency and selectivity. In such biological systems, a coordinated network of amino acid residues and water molecules typically facilitates the precise and timely delivery of protons, effectively forming a proton channel that supports the overall catalytic process. Introducing an acidic proton source into catalyst design to mimic this enzymatic strategy has recently been reviewed by Artero and Costentin in the context of hydrogen evolution and

Table 2 Comparison of the electrocatalytic CO_2RR performance of porphyrin-based bimetallic catalysts

Catalyst	Electrolyte solution	E^0_{cat}/(V *vs.* NHE), η (V)	% FE (CO)	k_{cat}/k_{obs}	log TOF_{max}	Ref.
10	MeCN, 3 M H_2O	−2, 1[a]	[b]92.3 (FE_{CH_4})	—	—	29
14	DMF, 1 M PhOH	−2.06[a], 0.75	79	—	7.43	33
15	DMF, 1 M PhOH	−1.91[a], 0.60	70	—	6.62	33
16	DMF, 10% H_2O	−1.35, 0.66	95	2.15×10^5 s^{-1}	3.60	34
18	DMF, 10% H_2O	−1.25, 0.56	92	1.60×10^4 s^{-1}	4.20	36
19	DMF, 10% H_2O	−1.60, 0.91	—	4.10×10^4 s^{-1}	5.80	36
20	DMF, 10% H_2O	−1.35, 0.69	—	7.30×10^5 s^{-1}	4.70	36
21	DMF/10% H_2O/1.0 M PhOH	−1.00, 0.26	98	4.30×10^6 s^{-1}	7.30	37

[a] For these systems the potentials are reported *vs.* Fc^+/Fc electrode and data were collected using secondary reference electrode. [b] This represents CO reduction to CH_4.

oxidation reactions. Their work provides valuable insights into the key parameters that govern proton delivery efficiency, including the positioning, pK_a, and mobility of the proton source within the catalyst's secondary coordination sphere.[40] In a pioneering work, Savéant's group, incorporated eight pendant hydroxyl groups in *ortho* positions of the phenyl rings of FeTPP, see catalyst **24** (Fig. 8).[5] The addition of these pendant proton donors led to improved CO_2-to-CO catalytic activity (log TOF_{max} = 5.97) at a reduced overpotential (η = 0.64 V) in DMF with 2 M H_2O, compared to Fe-TPP (catalyst **1**) under identical conditions (log TOF_{max} = 2.75 and η = 0.74 V). The study also demonstrated that substituting hydroxyl (–OH) groups with methoxy (–OCH_3) groups in catalyst **26** (Fig. 8) leads to significantly lower activity (log TOF_{max} = 2.7) and a much higher overpotential (η = 1.00 V). Furthermore, Warren and coworkers observed that having just one pendant hydroxyl group in catalyst **23** (Fig. 8) led to a marked decrease in catalytic activity (log TOF_{max} = 2.1 and η = 0.91 V).[41] This underscores the essential importance of a high local proton concentration near the catalytic centre. Again, the choice of the external proton source and solvent play a crucial role in determining the catalytic activity of this type of system. When 3 M phenol is used in DMF instead of water, catalyst **24** does not exhibit a notable performance enhancement (log TOF_{max} = 3.8 and η = 0.66 V), in fact that are still lower than those of Fe-TPP, which shows a log TOF_{max} of 4.5 and η' of 0.74 V.[42] The incorporation of electron-withdrawing fluorine atoms in catalyst **25** led to a slight reduction in overpotential (η = 0.59 V); however, its catalytic activity (log TOF_{max} = 4.0) remains lower than that of catalyst **1**.[42] This suggests that the pendant phenolic groups in catalysts **24** and **25** compete with bulk phenol for stabilizing the metal carboxylate intermediate. In contrast, with H_2O as the proton source, catalyst **24** provides a more localized acidic environment that directly interacts with the intermediate. Notably, switching the solvent from DMF to acetonitrile led to a marked increase in the catalytic activity of catalyst **23** (log TOF_{max} = 3.7) at a lower overpotential (η = 0.78 V).[41] Warren's group attributed this to DMF's stronger hydrogen-bond accepting ability, compared to MeCN, which interferes with the stabilization provided by the pendant phenolic groups.

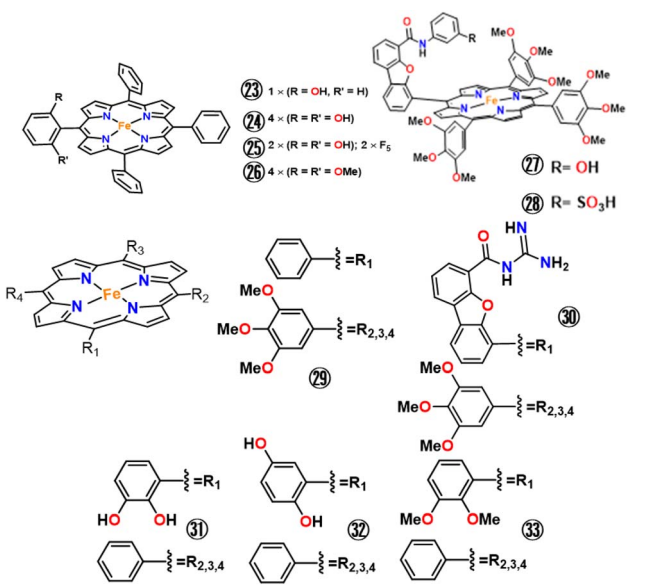

Fig. 8 Chemical structures of iron tetrephylporphyrin with local proton source.

Nocera's group explored local proton source effects using iron hangman porphyrins with pendant phenolic (catalyst **27**, Fig. 8) and sulfonic (catalyst **28**, Fig. 8) groups.[43] While –OH groups stabilized the CO_2 adduct by −5.0 kcal mol^{-1}, sulfonic groups (pK_a = 3) failed to enhance activity due to their inability to be reprotonated by weak external acids like PhOH (pK_a 18). Deprotonated sulfonates also caused steric and electrostatic misalignment, weakening CO_2 interaction. The reference catalyst **29** (Fig. 8), lacking pendant groups, showed similar activity, suggesting the dibenzofuran clefts in **27** and **28** is not well-suited for effective CO_2 binding.

Further, using their hangman cleft club with guanidine moiety in the secondary coordination sphere Nocera's group prepared another catalyst (catalyst **30**, Fig. 8) to perform CO_2 catalysis.[43] Electrochemical and subsequent DFT analysis revealed that for $2H^+/2e^-$ CO_2 reduction to CO the log TOF_{max} values were 2.71 and 2.47 s^{-1} for **27** and **30** respectively. On the other hand, CO binding stabilization Gibbs free energies were −6.62 kcal mol^{-1} and 2.13 kcal mol^{-1} for **27** and **30** respectively. Although, due to the presence of intramolecular hydrogen bonding for both these complexes, the CO_2 binding got favored to the Fe^0 state, but the dibenzofuran scaffold shown in this

work did not present the most optimized architecture for CO_2 association and hence rate of catalysis didn't improve much at low overpotential.

In this context, it's worth mentioning the work of Kondo and Masaoka *et al.*, where they successfully installed a hydroquinone (2,5-dihydroxyphenyl) moiety in the *meso*-position of simple iron porphyrin to synthesize catalyst **31** (Fig. 8).[44] Similarly, like the other examples **31** showed catalytic CO_2RR activity at 200 mV less overpotential compared to **1**, with 5% increase in catalytic current density. Controlled potential electrolysis showed at high η value, catalyst **31** could produce maximum 92% CO as product of CO_2RR with high catalytic rate, while maximum FE of 72% CO was produced by **1**, under the same electrochemical condition. When, they added externally hydroquinone moiety in the solution of catalyst **1** and performed the electrochemical analysis, similar increase in catalytic rate and selectivity was achieved. Through quantum chemical calculations, they showed the hydrogen bonding between the CO_2 adduct of iron to the hydroquinone moiety stabilized reactive intermediate and helped in catalysis.

However, Warren and co-workers realised in this work of Masoka *et al.* thermodynamically hydroquinone cannot act as electron donor and the relative positions between the hydroxy groups in the porphyrin hydroquinone preclude the possibility of both –OH groups to donate H^+ to the catalyst active site. Therefore for comparison, they used catechol (2,3-dihydroxyphenyl) pendant groups on top of porphyrins and synthesised Fe(CAT)TPP catalyst **33** (Fig. 8) along with its methyl protected version Fe(MeCAT)TPP catalyst **33** (Fig. 8) as a control.[45] When electrocatalysis was performed in DMF solvent using external proton source of 1 mM catechol, to make proper comparison of CO_2RR, it was found that **32** showed higher CO_2RR current compared to **1**, starting at 100 mV less onset potential. Catalytic rate for CO_2RR (k_{obs}) of **32**, was calculated to be 10-times higher than that of **1**, while 32 also showed improvement in k_{obs} value compared to 1, but not as much as that of **32** (contrary to the observation of Masaoka *et al.* about externally added quinol). It indicates the necessity of internal H-bond stabilizing group and H^+ source compared to that of external. Warren and co-workers further showed that their catalyst **32** was even ~3-times faster in rate compared to their single hydroxy catalyst **23** (Fig. 8), under identical condition of CO_2RR. The presence of the internal H-bond was proposed to facilitate the proton-coupled electron transfer process of carbon–oxygen bond breaking, which has been established as the rate-limiting step in CO_2-to-CO conversion. This inference was established, based-on primary kinetic isotope effect (pKIE) shown by catalysts **32** and **33** in CO_2RR (using PhOH/PhOD) to be 2.2, and 1.2, respectively. Further DFT calculation depicted, internal H-bonding in the pendant catechol stabilizes the intermediate of CO_2RR to facilitate the internal H^+-transfer more over external H^+-transfer in this case.

Overall, these studies demonstrate that strategically positioned local proton sources within the secondary coordination sphere are critical for enhancing CO_2RR activity and lowering overpotential in Fe-porphyrin catalysts. Efficient catalysis requires not only appropriate proton acidity (pK_a) but also precise spatial orientation and multiplicity of proton donors to enable intramolecular hydrogen bonding and proton-coupled electron transfer. Collectively, these results highlight that internal, well-organized proton relays outperform external proton sources, emphasizing the importance of secondary-sphere engineering in the rational design of next-generation CO_2RR catalysts. A comprehensive summary of the performance of all the catalysts discussed in this section is shown in Table 3.

2.5 Electrostatic effect

Through his groundbreaking research on enzyme function, Arieh Warshel clearly demonstrated that electrostatic effects are crucial in accelerating chemical reactions. He showed that electric fields or charged and polar groups within enzymes interact with the transition state, significantly lowering the activation energy and enhancing reaction rates. In [NiFe]-CODH or [Mo]-FDH (formate dehydrogenase), positive charge over the nearby amino acid residues plays a crucial role in stabilizing the charged COO-intermediates or transition states. Inspired by this facet of enzymatic functions, Savéant and co-workers designed an Fe-porphyrin by introducing trimethylammonium groups $-NMe_3^+$ in the *ortho* and *para* positions of the TPP-phenyl rings, respectively.[46] It was observed that the *ortho*-substituted porphyrin (**34**, Fig. 9) is the best for the CO_2RR as the negatively charged Fe^0–CO_2 intermediate is highly stabilized by the positively charged trimethylammonium groups *via* through-space electrostatic interactions resulting in a substantial reduction in overpotential (η = 0.22 V) along with a concurrent enhancement in turnover frequency ($\log TOF_{max}$ = 6).[47] Positioning the $-NMe_3^+$ groups at the *para* position resulted in catalyst (**35**, Fig. 9) showing a higher overpotential (η = 0.57 V) and reduced catalytic activity ($\log TOF_{max}$ = 4.4), emphasizing the importance of proper alignment of the positively charged groups for effective through-space electrostatic interactions.

This through-space electrostatic is further supported by the observed decrease in catalytic performance when the four $-NMe_3^+$ groups are replaced with four negative charges from $-SO_3^-$ groups positioned at the *para* locations on the TPP phenyl rings (**36**, Fig. 9).[46] These negatively charged sulfonate groups led to a lower catalytic activity ($\log TOF_{max}$ = 3.6) and a higher overpotential (η = 0.74 V), due to electrostatic repulsion with the negatively charged metal carboxylate intermediate. A similar result was seen with an iron hangman porphyrin with sulfonic acid groups (**37**, Fig. 9).[43] These groups were quickly deprotonated in solution, leading to electrostatic repulsion of the sulfonate group from the CO_2 intermediate.

Pushing this quest further, Nocera and co-workers synthesized a modified double hangman porphyrin bearing a pendant –COOH group and compared its activity with the single hangman porphyrin.[48] The CO_2 reduction reaction kinetics of *trans*-HP-(DCOOH)FeCl (**40**, Fig. 9) enable direct examination of electrostatic effects, as the pK_a of the pendant carboxylic acid group in DMF is estimated to be 13, sufficiently acidic that it does not accept a proton from added proton source (phenol). As

Table 3 Comparison of the electrocatalytic CO_2RR performance of Fe porphyrins bearing local proton source units

Catalyst	Electrolyte solution	E^0_{cat} (V *vs.* NHE), η (V)	% FE (CO)	k_{cat}/k_{obs}	log TOF_{max}	Ref.
1	DMF, 3 M PhOH	−1.41, 0.67	94	3.5×10^4 s^{-1}	4.5	5 and 42
1	DMF, 2 M H_2O	−1.41, 0.72	—	—	2.75	5
23	DMF, 1 M H_2O	−1.68[a], 0.95	—	1.33×10^2 s^{-1}	2.11	41
23	MeCN, 1 M H_2O	−1.9[a], 0.88	96	4.5×10^3 s^{-1}	3.7	41
24	DMF, 2 M H_2O	−1.333, 0.64	—	1.6×10^6 s^{-1}	5.97	5
24	DMF, 3 M PhOH	−1.35, 0.66	—	$>5 \times 10^6$ M^{-1} s^{-1}	3.8	42
25	DMF, 3 M PhOH	−1.28, 0.59	—	3×10^5 M^{-1} s^{-1}	4.0	42
26	DMF, 2 M H_2O	−1.69, 1.00	—	—	2.7	5
27	DMF, 0.04 M PhOH	−2.13[a], —	94	2.23×10^3 M^{-1} s^{-1}	2.71	43
28	DMF, 0.04 M PhOH	−2.15[a], —	96	6.58×10^2 M^{-1} s^{-1}	2.18	43
29	DMF, 0.04 M PhOH	−2.2[a], —	99	2.8×10^3 M^{-1} s^{-1}	2.81	43
30	DMF, 0.04 M PhOH	2.15[a], —	93	1.28×10^3 M^{-1} s^{-1}	2.47	43
31	γ-Butyrolactone, 2 M H_2O	−1.89, —	92[b]	—	—	44
32	DMF, 0.01 M PhOH	−2.35[a], —	89	4.8×10^2 s^{-1}	—	45
33	DMF, 0.01 M PhOH	—, —	—	1.0×10^2 s^{-1}	—	45

[a] For these systems the potentials are reported *vs.* Fc^+/Fc electrode and data were collected using secondary reference electrode. [b] Bulk electrolysis performed in MeCN.

a result, a negative charge in the secondary coordination sphere is preserved throughout the entire catalytic cycle. The negative charge has a negative impact on the rate-determining step, leading to a decrease in catalytic current in the order: **38** > **39** > **40** (Fig. 9). Again, in single-hangman version, CO_2 effortlessly binds to the opposite face, keeping CO_2RR rates comparatively high, much like an unmodified porphyrin. But in the α,β-isomer of the double hangman system, the unavoidable negative charge in the secondary coordination sphere drags down the catalytic rate for CO_2RR. These results shine light on how disruptive nonbonding electrostatic interactions can hinder CO_2RR catalysis, highlighting the need to control these destabilizing forces for achieving top-tier catalytic performance.

To gain deeper mechanistic insight into the beneficial influence of ionic liquids on the selective two-electron/two-proton reduction of CO_2 to CO, our group developed a modified iron porphyrin (**41**, Fig. 9) bearing methylimidazolium substituents on the periphery of the porphyrin ring.[16] In general, it was observed that most electrocatalytic investigations were carried out in organic solvents with the addition of

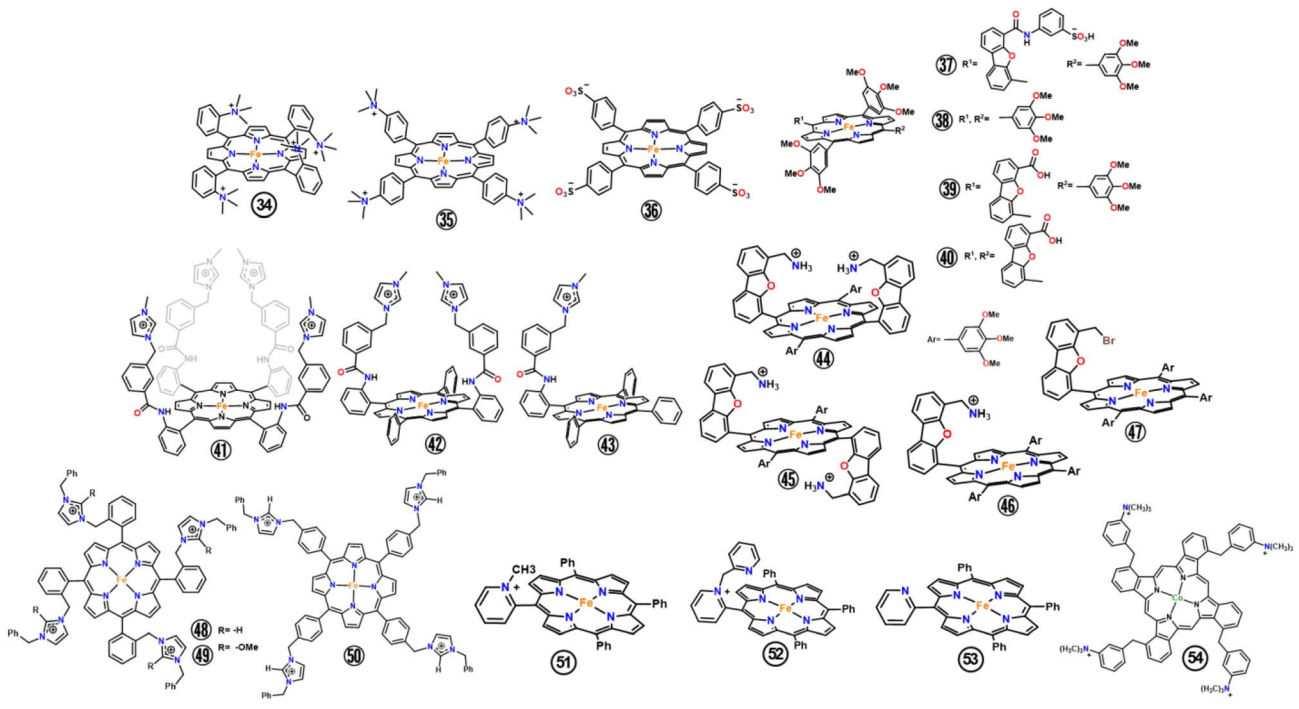

Fig. 9 Modified iron-porphyrins with electrostatic groups in secondary coordination sphere.

a sacrificial proton donor (such as trifluoroethanol, water, or phenol). Typically, introducing water as a proton source led to a notable enhancement of the catalytic current at lower overpotentials. However, when the water concentration increased beyond a certain level, a sharp decrease in the catalytic current accompanied by positive potential shifts was observed. The resulting tetracationic complex (**41**) is water-soluble, enabling evaluation of its catalytic behavior for CO_2 reduction in water, a clean and convenient solvent that simultaneously serves as a proton source. The cyclic voltammogram (CV) of complex **41** in Ar-saturated aqueous solution containing 0.1 M KCl displays three redox processes similar to those recorded in DMF. Interestingly, despite the lower solubility of CO_2 in water (0.033 M) compared to DMF (0.23 M), a significantly higher catalytic current was observed for CO_2 reduction at a much lower potential ($(E^0_{cat}) = -1.018$ V *vs.* NHE). This enhanced electrochemical reactivity relative to that in DMF was attributed to the stabilization of the key $[Fe(por)CO_2]^{2-}$ intermediate through coulombic interactions with the positively charged methylimidazolium groups. In water, with its higher dielectric constant ($\varepsilon_r = 78.4$) compared to DMF ($\varepsilon_r = 36.7$), the dissociation of the methylimidazolium$^+Cl^-$ units is more extensive, resulting in stronger electrostatic stabilization of the intermediate *via* more effective space-charge interactions with the "free" cationic groups. Controlled potential electrolysis (CPE) experiments revealed that the catalyst exclusively produces CO with a FE of 91%, with no detectable formation of H_2 or HCOOH. The rate constant (k_{cat}), turnover frequency (TOF), and turnover number (TON) were determined to be 2.44×10^5 s^{-1}, 1.50×10^4 s^{-1} ($\log TOF = 4.18$), and 1.08×10^8, respectively. Notably, these electrocatalytic parameters obtained in aqueous medium surpass those reported for **1** in DMF containing 1 M tetrafluoroethanol as proton source and 0.3 M methylimidazolium-type ionic liquid at an overpotential of 870 mV.

In another study, a series of tetra-(**41**), di-(**42**), and mono-(**43**) substituted iron porphyrins with cationic imidazolium groups were explored towards CO_2RR (Fig. 9).[16,49] Here, these groups in the second coordination sphere also help to stabilize the Fe–CO_2 intermediate through electrostatic interactions. It was found that the electrocatalytic overpotential depends on the number of imidazolium groups present. Notably, a six-order-of-magnitude increase in turnover frequencies was observed when transitioning from a tetra ($TOF_{max} = 3.10 \times 10^2$ s^{-1}) to a mono ($TOF_{max} = 2.05 \times 10^8$ s^{-1}) substituted catalyst. Additionally, the comparative study revealed that the catalytic performance driven by through-space electrostatic interactions outperforms the traditional through-structure electronic effect.

In contrast to the above study, Cao and co-workers reported efficient catalytic CO_2 reduction using iron porphyrins decorated with two cationic *N*,*N*,*N*-trimethylbenzylammonium groups arranged in either *cis* (**44**) or *trans* (**45**) configurations through dibenzofuran linkages.[50] They concluded that CO_2RR activity increased, asevidenced by higher catalytic currents and lower onset potentials, with an increasing number of cationic substituents.

These Fe porphyrins were shown to be highly active and selective for electrocatalytic CO_2-to-CO conversion in acetonitrile using phenol as the proton source. Notably, the *cis*-isomer outperformed the *trans*-isomer, achieving a TOF_{max} of 4.4×10^5 s^{-1}. Both dicationic systems exhibited substantially higher reactivity than their monocationic (**46**) and non-cationic (**47**) analogues. Overall, the CO_2RR activity followed the order **44** > **45** > **46** > **47**.

Complex **45** contains two cationic units positioned on opposite sides of the porphyrin plane. Consequently, relative to **46**, CO_2 binding and activation can occur on both faces of the macrocycle, rendering **45** significantly more active for CO_2RR. In contrast, in complex **44** both cationic units are located on the same side of the porphyrin plane, leaving the opposite face unfunctionalized. The superior activity of **44** compared with **45** indicates that cooperative interactions between the two proximal cationic units play a decisive role in further enhancing CO_2RR.

DFT calculations revealed that the Fe^0 species of **44** can readily bind a CO_2 molecule to form a formal Fe^I–$CO^{\bullet -}$ intermediate with a low activation free energy barrier of 3.3 kcal mol^{-1}, whereas CO_2 binding in **45** proceeds with a significantly higher barrier of 6.1 kcal mol^{-1}. Importantly, in the transition state for **44**, one cationic unit stabilizes the "pseudodissociative" hydroxide of the COOH moiety, while the second interacts electrostatically with the phenolate anion. By contrast, in the transition state of **45**, the single cationic unit engages only with the phenolate anion.

This spatial arrangement enables simultaneous stabilization of key reaction intermediates and charged species within the secondary coordination sphere, thereby lowering the overall energetic requirements for CO_2 activation and reduction. This work thus compellingly demonstrates a role-specialized, cooperative strategy for enhancing molecular CO_2 reduction catalysis.

Chang and co-workers inserted second-sphere imidazolium pendants over a Fe-porphyrin that exhibit multifunctional charge and hydrogen-bonding effects, enhancing the capture and electrochemical reduction of CO_2.[51] In the presence of 2,2,2-trifluoroethanol (TFE) as a proton source, under a CO_2 atmosphere, catalyst **48** (Fig. 9) demonstrates the highest catalytic current and the most positive onset potential for catalysis, followed by **49** (Fig. 9), while **50** (Fig. 9) shows the lowest activity among the three catalysts. The TOF values observed for catalyst **48** with 3.0 M TFE (1.3×10^9 s^{-1}) represent a 14 000-fold increase compared to the **50** congener (8.7×10^4 s^{-1}) and a 2000-fold increase compared to **1** in MeCN (6.5×10^5 s^{-1}). However, this is only a 40-fold increase over **49** derivative (3.2×10^7 s^{-1}), which retains the imidazolium positive charge but lacks the C_2–H hydrogen-bonding capability. These results suggest that electrostatic effects play a more significant role in catalytic amplification than hydrogen-bond interactions in this case. This work highlights that while hydrogen-bonding aids in CO_2 capture, the primary source of catalytic enhancement comes from the nearby electrostatic interactions.

An intriguing study by Dey and colleagues explored the CO_2 reduction capabilities of various iron porphyrin complexes in

an organic solvent, using water as the proton source.[52] The catalysts included: catalyst **10** (Fig. 5), featuring pendant pyridines that enable hydrogen bonding (HB) through a water molecule; catalyst **51** (Fig. 9), containing quaternary pyridinium groups that introduce electrostatic interactions (ESI); catalyst **52** (Fig. 9), which incorporates both HB and ESI functionalities; and catalyst **53** (Fig. 9), lacking both HB and ESI. Both HB and ESI significantly enhanced the selective $2e^-/2H^+$ reduction of CO_2 to CO, achieving FE greater than 90% at water concentrations below 2% (v/v). Notably, the HB-driven system maintained high selectivity across a wide range of water concentrations, indicating its robustness to proton availability. In contrast, the ESI-based system showed high selectivity only at low water content; at higher water concentrations, its performance declined, favoring H_2 evolution instead. Specifically, the ESI catalyst produced more than 85% H_2 in a CO_2-saturated solution containing 5% (v/v) water. The underlying cause of the sharp drop in CO_2 reduction selectivity at higher water concentrations was investigated using time-correlated single photon counting (TCSPC) and molecular dynamics (MD) simulations. These studies revealed that the cationic quaternary pyridinium moiety becomes increasingly solvated as water concentration rises. This solvation effect significantly prolongs the residence time of water molecules near the catalyst, thereby favoring proton (H^+) reduction over CO_2 reduction. As a result, the iron porphyrin predominantly forms an Fe–H intermediate. This intermediate can either undergo protonation to yield H_2 or react with CO_2 to form HCOOH. The pathway taken for H_2 *vs.* HCOOH production is ultimately governed by the hydricity of the Fe–H species. These findings indicate that the catalytic influence of electrostatic secondary interactions can only be effectively observed in hydrophobic environments such as buried protein active sites or organic solvents, since introducing water into these systems leads to elevated local water concentrations around the catalyst. Placing ESI in the catalyst isn't just about adding charge—it's about playing with water as well. Its ability to draw in and organize surrounding water molecules can add a twist to the chemistry, making precise positioning key to unlocking catalytic performance.

In a notable study, Warren and co-workers showed that incorporating cationic *N*,*N*,*N*-trimethylammonium-phenoxy groups near the cobalt center in cobalt phthalocyanine (CoPc) can significantly enhance its catalytic performance.[53] First of all, the trimethylammonium-phenoxy groups in compound (**54**, Fig. 9) make the catalyst water-friendly. These charged, hydrophilic arms dramatically boost solubility in aqueous media and prevent the usual aggregation issues that plague CoPc, keeping the catalyst dispersed, active, and ready for action. However, the key to the enhanced reactivity lies in the flexible trimethylammonium-phenoxy groups, which serve a dual role: they provide electrostatic stabilization to the reduced Co–CO_2 intermediates and contribute a high local positive charge density that promotes CO_2 binding and reduction. Impressively, analysis of cyclic voltammetry (CV) data reveals CO_2 reduction rate constants up to 1000 times higher than those reported for heterogeneous CoPc systems and comparable to the best homogeneous metalloporphyrin catalysts. A comprehensive summary of the performance of all the catalysts discussed in this section is shown in Table 4.

Collectively, these studies underscore that electrostatic interactions within the secondary coordination sphere are a powerful lever for enhancing CO_2RR activity, lowering overpotentials, and accelerating key reaction steps. Precisely positioned cationic groups stabilize negatively charged intermediates and transition states through through-space coulombic effects, while misaligned or persistent anionic charges can be strongly detrimental. Importantly, the balance between electrostatics, solvation, and proton management emerges as a decisive design principle, highlighting that effective catalyst engineering requires not just charging introduction, but its spatial organization and environmental compatibility.

2.6 Entatic state model

A fundamental feature underlying the remarkable reactivity of several biological metalloenzymes is the concept of the entatic state. In this state, the protein environment imposes a geometrically or electronically strained configuration on the metal center. Positioning it in a strained, high-energy configuration that is preorganized for reactivity. Rather than allowing the metal to adopt its thermodynamically favored structure, the enzyme holds it in a catalytically "primed" form, poised to undergo chemical transformation with minimal reorganization energy.

A classic example is found in type-1 copper sites of blue copper proteins, where the copper center is held in an unusual, distorted tetrahedral geometry by the surrounding protein ligands, enhancing its ability to shuttle electrons with minimal structural change. The electron self-exchange rate constants (k_{11}) for various blue copper proteins, each featuring a single type-1 copper center, typically fall within the range of 10^5 to 10^8 M^{-1} s^{-1}. In contrast, most synthetic Cu(II)/Cu(I) inorganic complexes display significantly lower k_{11} values, generally ranging from 10^0 to 10^4 M^{-1} s^{-1}. Similarly, in cytochrome c oxidase, the binuclear center involving heme iron and copper operates in a preorganized entatic configuration that facilitates O_2 binding and reduction. These biological insights have inspired synthetic chemists to incorporate entatic principles into the design of artificial catalysts, where applying controlled geometric or electronic strain can mimic enzyme-like efficiency and selectivity. Understanding and harnessing the entatic state offers a powerful strategy for bridging the gap between biological and synthetic catalysis.

The reported model systems for electron transfer proteins are not limited to the entatic state concept; they display a broad spectrum of ligand geometries and donor types. So far, the fastest electron transfer rates reported reach between 10^5 to 10^6 M^{-1} s^{-1}. Several non-heme complexes featuring both nitrogen and sulfur donor atoms have been studied to explore the entatic state. However, direct evidence of how these unique characteristic influences catalysis, especially CO_2 reduction is still missing. In CO_2 reduction, where multi-electron transfer steps are often involved, a high electron self-exchange rate ensures

Table 4 Comparison of the electrocatalytic CO_2RR performance of Fe porphyrins bearing electrostatic units

Catalyst	Electrolyte solution	E^0_{cat} (V *vs.* NHE), η (V)	% FE (CO)	k_{cat}/k_{obs}	log TOF_{max}	Ref.
34	DMF, 3 M PhOH	−0.944, 0.25	100	—	6	46
35	DMF, 3 M PhOH	−1.26, 0.57	93	—	4.4	46
36	DMF, 3 M PhOH	−1.42, 0.74	—	—	3.6	46
37	DMF, 0.04 M PhOH	−2.15[a], —	96	6.58×10^2 M^{-1} s^{-1}	2.18	43
38	DMF, 0.04 M PhOH	−2.2[a]	100	2.80×10^3 M^{-1} s^{-1}	2.81	48
39	DMF, 0.04 M PhOH	−2.15[a]	100	1.57×10^3 M^{-1} s^{-1}	2.56	48
40	DMF, 0.04 M PhOH	−2.2[a]	100	1.11×10^2 M^{-1} s^{-1}	1.41	48
41	DMF, 5.5 M H_2O	−0.969, 2.29	91	3.10×10^2 s^{-1}	2.49	16 and 49
42	DMF, 5.5 M H_2O	−1.168, 4.28	93	8.57×10^5 s^{-1}	5.93	16 and 49
43	DMF, 5.5 M H_2O	−1.357, 6.17	89	2.05×10^8 s^{-1}	8.31	16 and 49
44	MeCN, 0.2 M PhOH	−1.82[b], —	95	4.4×10^5 s^{-1}	5.64	50
45	MeCN, 0.2 M PhOH	−1.88[b], —	93	2.4×10^5 s^{-1}	5.38	50
46	MeCN, 0.2 M PhOH	−1.98[b], —	93	8.9×10^4 s^{-1}	4.94	50
47	MeCN, 0.2 M PhOH	−2.05[b], —	91	2.1×10^4 s^{-1}	4.32	50
48	MeCN, 3 M TFE	−1.78[a], 0.24	100	—	9.1	51
49	MeCN, 3 M TFE	−1.79[a]	100	—	7.5	51
50	MeCN, 3 M TFE	−1.79[a]	28	—	4.9	51
51	MeCN, 1% H_2O	−2.15[a]	93.8	—	0.40	52
52	MeCN, 1% H_2O	−2.15[a]	90.6	—	1.15	52
53	MeCN, 5% H_2O	−2.20[a]	26.8	—	—	52
54	pH 7, 0.1 M KCl	−1.2 V *vs.* RHE, 0.56	59	~10^7	4.7	53

[a] For these systems the potentials are reported *vs.* Fc^+/Fc electrode and data were collected using secondary reference electrode. [b] Value represents the onset potential of catalytic current.

smooth coordination between electron flow and substrate activation, leading to higher catalytic turnover and selectivity. Exploring this aspect could unlock new pathways to design faster, more efficient, and sustainable CO_2 conversion catalysts.

2.7 Structural dynamics

Understanding the nature of the active site of the catalyst is crucial for precisely controlling reaction kinetics and dynamics. However, determining the geometry and electronic structure of the active site is complex, as they are influenced by numerous factors—including nature of metal centre, coordinating atoms, coordination numbers, and secondary coordination environment. These variables make it difficult to establish clear structure–activity relationships and to uncover the detailed reaction mechanisms. Adding to the complexity is the fact that active sites often undergo dynamic changes during catalysis. Their structures can be altered by external conditions such as temperature, electrochemical potential, and experimental setup. This dynamic behaviour complicates efforts to pinpoint the true catalytic structure and to correlate structure with catalytic performance. As a result, there is a growing need for techniques that enable real-time monitoring of the structural evolution of active sites under realistic operating conditions. Such capabilities are essential for achieving an atomic-level understanding of catalytic processes as they occur. The advancement of *in situ* and *operando* techniques—such as X-ray absorption spectroscopy (XAS), Fourier-transform infrared spectroscopy (FT-IR), and Raman spectroscopy, has opened new avenues for identification of active sites, detection of reaction intermediates, and elucidation of catalytic mechanisms.

A particularly inspiring example of structural dynamics can be found in enzymatic systems. In formate dehydrogenase, for instance, a selenocysteine ligand bound to the Mo center can transiently dissociate, acting as a base to deprotonate formate during its conversion to CO_2. This type of ligand mobility, where a group shuttles between inner- and outer-sphere coordination, demonstrates how dynamic structural rearrangements can directly enhance catalytic turnover.

Smith and co-workers addressed this challenge by designing an iron porphyrin complex in which a carboxylate group was covalently tethered to the macrocycle.[54] The complex **55** (Fig. 10) was evaluated for CO_2 electroreduction in DMF with water as the proton donor. Remarkably, its turnover frequency was found to be four orders of magnitude higher than that of the benchmark catalyst **56** (Fig. 10) under similar overpotentials. Here it is worth mentioning that increasing the number of *meso*-pentafluorophenyl substituents renders Fe porphyrins less active and selective for CO_2RR in DMF. Strong electron-withdrawing *meso*-substituents make the central Fe center more electron-deficient, which weakens CO_2 binding to the

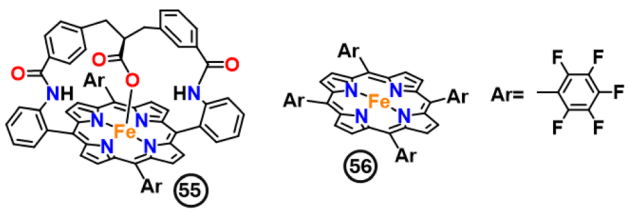

Fig. 10 Chemical structures of iron porphyrin complex in which a carboxylate group was covalently tethered to the macrocycle.

catalytically active Fe^0 state. Thus, although such substituents shift the catalytic wave anodically, they simultaneously reduce metal-center electron density and consequently diminish CO_2 binding affinity.[55] In **55**, a strong kinetic isotope effect (KIE ≈ 4.5) indicated that proton transfer is implicated in the rate-determining step. Water emerged as the most efficient proton source, suggesting that a hydrogen-bonding network plays an important role in proton delivery during catalysis. The enhanced reactivity was attributed to the dynamic behavior of the carboxylate group: it can vacate the metal coordination site and function as a proton relay in the secondary coordination sphere. This structural flexibility provides a clear example of how incorporating mobile ligating groups into molecular scaffolds can significantly improve catalytic efficiency for CO_2RR.

In summary, structural dynamics represent a powerful but underexplored dimension in the design of molecular CO_2 reduction catalysts. Looking ahead, the field will benefit from systematic efforts to design catalysts with built-in flexibility, where ligating groups or proton relays can reversibly move in and out of the coordination sphere to accelerate key elementary steps. Coupling such rational design with advanced *in situ* and *operando* spectroscopic tools will be essential to directly observe these dynamic events under catalytic conditions. Future research is expected to not only deepen the mechanistic understanding of ligand dynamics but also establish general design principles, paving the way for next-generation molecular catalysts that combine efficiency, selectivity, and robustness for sustainable CO_2 conversion.

2.8 C_2 product formation in homogeneous CO_2 electrocatalysis

Direct generation of C_2 products, from CO_2 reduction to produce components of natural gas, were previously mainly limited to heterogeneous metal-based catalysts. Very recently, the pioneering work of Dey and co-workers breached this barrier for molecular homogeneous catalysts, where with mononuclear iron porphyrin having 2nd sphere pendant thiol moieties (**57**, Fig. 11), they were able to get ethane (C_2H_6) as the product of CO_2RR.[56] They inherited this idea from natural enzyme methionine synthase where a thiol head group from a homocysteine residue picks up a $-CH_3$ group from the $-CH_3$ bound cobalt(III) corrin cofactor, which is invoked in the synthetic complexes by Patra *et al.* in this work. Under homogeneous electrochemical condition of CO_2 saturated CH_3CN solution and in presence of 2.5 M H_2O as proton source, **57** was shown to reduce CO_2 *via* $14e^-/14H^+$ reduction to produce 32% FE of ethane at −2.0 V *vs.* Ag/AgCl from its formal Fe^0 state, and the formation of ethane was confirmed from $^{13}CO_2$ experiments. When they varied the conc. of H_2O (from 0.5 M to 5 M), a systematic increase in FY of ethane from 13% to 40% was obtained, while the other major product CO got decreased from 83% to 57% (further increase in H_2O conc. decreased FY of C_2H_6 due to solubility issue). They also tried structural variation, by decreasing the chain length (**58**, Fig. 11), increasing number of thiol groups (**59**, Fig. 11), and in both cases decrease in FY of C_2H_6 at the expense of CO was observed, indicating the fact that optimum distance of the 2nd sphere thiol group is key to C_2H_6 formation. In the mechanism for ethane formation, Dey and co-workers proposed a possibility of RS-H insertion in an iron porphyrin carbene (IPC), *i.e.*, Fe=CH_2, being the key pathway. With one CO_2 molecule $FeTPPC_2SH$ (**57**) underwent $4e^-/6H^+$ reduction to form Fe=CH_2 carbene first, in which step second sphere thiol group made a nucleophilic attack to the electrophilic carbene to form thioether rendering the iron center vacant. This methyl transfer was only possible due to the presence of thiol group in the 2nd sphere, which they termed as "parking space" for methyl group. The next key step in the probable mechanism was after $6e^-/7H^+$ of another CO_2 molecule by the iron porphyrin, the nucleophilic attack of iron bound methyl group to the thioether sitting in the second sphere to complete C–C bond formation yielding ethane. Although, they were not able to trap the carbene intermediate in this study, but thiol attack to IPC were previously reported by Fasan and co-workers.[56] In addition to that, by separately synthesizing iron porphyrin with a pendant ethyl thioether ($FeTPPC_2SEt$) and reacting with chemically generated Fe^{II}–CH_3 (UV features at 361, 431, 501, 612, and 710 nm), they proved the C–C bond formation step ultimately generating Fe^{II}, monitored in UV-vis spectroscopy. This work reported a unique design strategy taking inspiration from methyl transferases, for selective C_2H_6 formation from CO_2RR.

Secondary coordination sphere (SCS) engineering has emerged as a powerful strategy to enhance the efficiency, selectivity, and mechanistic control of CO_2 reduction catalyzed by iron porphyrins. By mimicking key features of metalloenzymes, modifications such as hydrogen-bonding functionalities, proximal proton relays, bimetallic cooperativity, and local electrostatic fields significantly modulate the electronic environment and reactivity of the metal center. These non-covalent and spatially tuned interactions help stabilize key intermediates, lower activation barriers, and facilitate concerted proton–electron transfer processes essential for CO_2 conversion to value-added products. Among the strategies discussed, urea- or amide-based H-bond donors offer substrate preorganization, pendant acidic/basic groups enable efficient proton delivery, bimetallic frameworks introduce cooperative redox or Lewis acid effects, while charged substituents fine-tune redox potentials and local pK_a.

Despite these advances, a fundamental understanding of entatic state, the structural dynamics of the catalyst during the reaction still remains incomplete. Future work should focus on this direction. Expanding the chemical diversity of SCS elements and integrating *operando* spectroscopic and

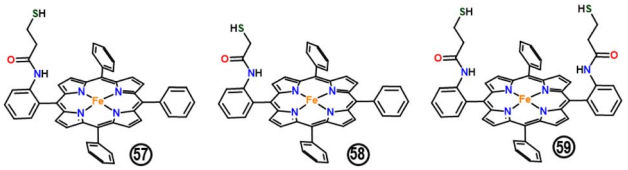

Fig. 11 Chemical structures of the iron porphyrins having pendant thiol residues, used for ethane formation by Dey and co-workers.[56]

electrochemical techniques will be vital for rational catalyst design. Ultimately, SCS modification offers a biomimetic blueprint for advancing molecular CO_2 reduction catalysis, moving toward sustainable and efficient carbon management technologies.

3 Bio-inspired molecular catalysts for heterogeneous CO_2 electrocatalysis

As detailed in Section 1, homogeneous electrochemical CO_2 reduction has predominantly been performed in organic media, primarily owing to the limited solubility of molecular catalysts in aqueous environments. Nevertheless, this strategy is frequently hindered by the formation of catalytically inactive dimeric species in solution, resulting in diminished catalytic efficiency.[57] Moreover, homogeneous systems pose substantial challenges for catalyst-product separation, complicating post-reaction processing.[58] To overcome these inherent drawbacks and to enhance both the catalytic activity and long-term stability of the system, molecular catalysts have been covalently or noncovalently anchored onto conductive solid supports to construct hybrid electrodes. This immobilization strategy gives rise to a heterogeneous electrocatalytic platform for CO_2 reduction, combining the molecular level tunability of homogeneous catalysts with the practical advantages of heterogeneous systems.

3.1 Metalloporphyrin in H-cell configuration

The earliest class of molecular complexes investigated for CO_2 electroreduction comprised metalloporphyrins. In a representative study, Daasbjerg and co-workers employed cobalt *meso*-tetraphenylporphyrin (**60**), the structure shown in Fig. 12 as a model system to comparatively examine its catalytic behavior under homogeneous and heterogeneous conditions.[59] Upon immobilization of catalyst **60** onto carbon-based supports-specifically carbon nanotube (CNT) and carbon black (CB) carrier-a substantial enhancement in electrocatalytic performance was observed. The system achieved a maximum FE for CO formation of 91% at −1.35 V *vs.* SCE with a current density of −3.2 mA cm^{-2} when CNT was used as the support, and 97% FE at a current density of −1.9 mA cm^{-2} with CB. These variations are attributed to differences in the intrinsic porosity and surface area of the carbon materials, which affect the local concentration of catalytically active **60** species. Notably, the superior performance observed with CNT-supported **60** is believed to stem from the distinct electronic structures of the catalytic intermediates under different conditions: $[Co^{0}TPP]^{2-}$ in homogeneous system *versus* $[Co^{I}TPP]^{-}$ in the heterogeneous configuration.

A detailed mechanistic investigation into the stability of **60** immobilized on carbon cloth was conducted by Jiang *et al.*[60] In a series of three consecutive 4 h electrolysis experiments performed at −1.05 V *vs.* NHE, a progressive decline in catalytic performance was observed. Specifically, the turnover frequence (TOF) decreased from 9.1 ± 3.8 s^{-1} to 5.1 ± 3.6 s^{-1} by the end of the third run, while the FE_{CO} dropped from 80 ± 6.8% at the beginning to 64 ± 14.3%. The study identified two principal degradation mechanisms contributing to catalyst deactivation: oxidative degradation induced by CO_2 and reductive carboxylation. In the oxidation pathway, formation of $[Co^{III}TPP]OH$ species was found to be kinetically stabilized under reductive potentials, likely due to a substantial reorganization energy barrier associated with the –OH elimination. In the reductive pathway, the dianionic species $[Co^{0}TPP]^{2-}$ and its carbonylated counterpart $[Co^{0}TPP\text{-}CO]^{2-}$ acted as key intermediates, which readily underwent irreversible reactions with CO_2. These processes ultimately resulted in the structural disintegration of the catalyst framework, thereby accounting for the observed loss in catalytic activity.

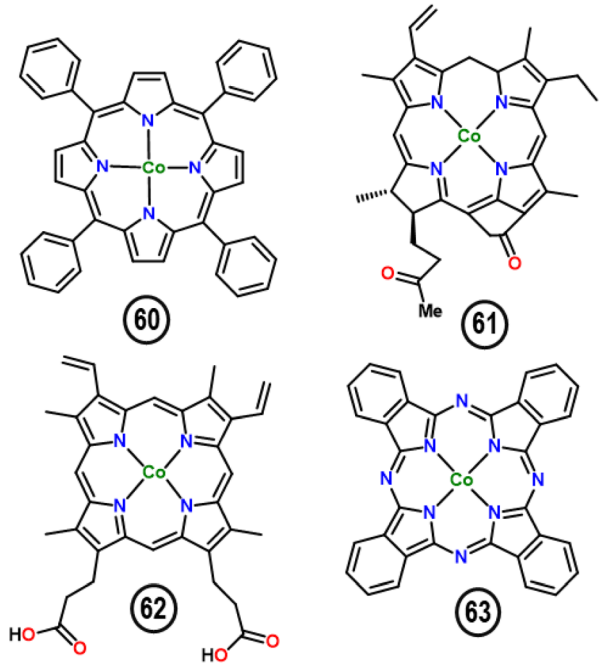

Fig. 12 Chemical structures of tetraphenylporphyrin **60**, cobalt chlorin **61**, cobalt metalloprotoporphyrin **62**, cobalt phthalocyanine **63**.

Recent work by Cao *et al.*[61] employs a bicomponent electrocatalyst, using structurally related molecules with Co (catalyst **60**) and Cu metal centers for selective CO and H_2 production, respectively, to generate syngas with a tunable H_2/CO ratio (0.1–6.4). Fukuzumi *et al.* investigated the electrochemical reduction of CO_2 to CO in aqueous solution using a cobalt chlorin (**61**) complex immobilized on multi-walled carbon nanotubes (MWCNTs).[62] Under optimized conditions (−1.1 V *vs.* NHE at pH 4.6), the system achieved a FE_{CO} of 89%, with the remaining 11% accounting for the H_2 production. The catalyst exhibited a maximum turnover number (TON) of 1500 and TOF of 100 h^{-1}. Electron paramagnetic resonance (EPR) spectroscopy suggested that the high selective toward CO formation arises from a cooperative two-electron transfer process involving two Co(I) species. When MWCNTs were substituted with reduced graphene oxide (rGO) as the support, a notable decline in catalytic performance was observed, with the TON reduced to 300. This

performance disparity was attributed to the unique three-dimensional architecture of MWCNTs, which facilitates effective catalyst dispersion and electron transfer. Furthermore, π–π interactions between Co^{II}(Ch) and the conjugated surfaces of MWCNTs were identified as a critical factor enhancing the selective CO_2-to-CO conversion.[63–65]

Marc Koper's group investigated the electrochemical reduction of CO_2 catalyzed by cobalt protoporphyrin (**62**, structure shown in Fig. 10) immobilized on pyrolytic graphite.[66] The catalytic activity exhibited a pronounced dependence on pH. At pH 1, the FE_{CO} was relatively low, amounting to only a few percent, with H_2 evolution being the predominant process. However, under moderately acidic conditions (*e.g.*, pH 3), CO emerged as the principal product, with an FE of approximately 40%. Minor amounts of formic acid and methane were also detected at pH 1 but were absent at higher pH values, indicating a shift in reaction selectivity. These observations underscore the critical role of the initial electron transfer to CO_2 in determining the catalytic pathway. Specifically, the formation of a surface-bound $CO_2^{\bullet-}$ radical anion intermediate initiates the reduction process. This species exhibited strong Brønsted basicity and can readily accept a proton from water, leading to a mechanistic profile that is highly sensitive to pH and distinct from that of the competing hydrogen evolution reaction.

Koper and co-workers further examined how variations in the central metal atom and carbon support of immobilized metallo-protoporphyrins influence their catalytic behavior toward the electrochemical reduction of CO_2 to formic acid.[67] In this study, a series of metallo-protoporphyrins were immobilized on pyrolytic graphite electrodes and tested in perchloric acid at pH 3. Based on their catalytic performance, the complexes were categorized into three groups: (i) Cr, Mn, Co, and Fe protoporphyrins, which showed no detectable formation of formic acid; (ii) Ni, Pd, Cu, and Ga analogues, which produced only trace amounts; and (iii) Rh, In, and Sn complexes, which yielded significant quantities of formic acid, with faradaic efficiencies ranging from 1% to as high as 70%, depending on the metal center. Theoretical work showed that nature of the nucleophile attacking the carbon atom of CO_2, determines the selectivity between CO or $HCOH/HCOO^-$.[68] The electrogenerated nucleophile can be the reduce metal center, the metal-hydride or phlorin-hydride ligand.[69]

Early metalloporphyrin complexes established foundational structure–function relationships for CO_2 electroreduction. These studies demonstrated that catalytic performance and selectivity are critically governed by the choice of metal center, the method of catalyst immobilization, and the nature of the carbon support, which collectively modulate electronic structure and reaction pathways.

3.2 Metallo phthalocyanine in H-cell configuration

Another prominent class of molecular catalysts investigated for CO_2 electroreduction is metal phthalocyanines. Among these, cobalt phthalocyanine (**63**) has garnered significant attention due to its favorable characteristics, including synthetic accessibility, high chemical stability, and the capacity for molecular-level structural modification. These features make cobalt phthalocyanine-based systems particularly attractive for catalyst design and mechanistic studies. A summary of recent literature reports on the electrocatalytic performance of various **63** loaded materials for the selective reduction of CO_2 to CO is presented in Table 5.[70]

The nature of the support material plays a crucial role in determining the catalytic performance of heterogeneous systems for electrochemical CO_2 reduction.[78] Zhuang and co-workers systematically compared two widely used carbon-based supports—Vulcan XC-72 and carbon nanotubes (CNTs)—for the immobilization of cobalt phthalocyanine (**63**). Both **63**/XC-72 and **63**/CNTs exhibited high selectivity and long-term operational stability for CO generation. In the case of **63**/XC-72, electrolysis at a constant current density of 10 mA cm^{-2} yielded a stable cathodic potential within a fluctuation range of less than 40 mV over the first 15 hours, achieving a turnover number (TON) of 48 600. The FE for CO (FE_{CO}) remained above 84%, with an average turnover frequency (TOF) of 0.9 s^{-1}. For the **63**/CNTs system, enhanced durability was observed, with polarization remaining steady over 45 hours and a corresponding TON reaching 180 000. The FE_{CO} consistently exceeded 88%, accompanied by an average TOF of 1.0 s^{-1}. This enhanced performance was attributed to the homogeneous dispersion of **63** molecules on CNTs and strong π–π interactions facilitating electron transfer.

Wang and co-workers developed a hybrid electrocatalyst by uniformly anchoring catalyst **63** onto carbon nanotubes (CNTs) for the electrochemical reduction of CO_2.[78] In 0.1 M $KHCO_3$ aqueous electrolyte, the **63**/CNT composite achieved a current density exceeding 10 mA cm^{-2} at an overpotential of 0.52 V, accompanied by a FE_{CO} greater than 90%, corresponding to a turnover frequency of 2.7 s^{-1}. During prolonged electrolysis at −0.63 V *vs.* RHE, the system maintained a stable current density of approximately 10 mA cm^{-2} for 10 hours, with FE_{CO} consistently above 90%, yielding a turnover number of 97 000 for the CO_2 to CO conversion. For comparative analysis, **63** was also immobilized on reduced graphene oxide (rGO) and carbon black (CB). Under identical conditions (−0.59 V *vs.* RHE), both **63**/rGO and **63**/CB exhibited less than one-third of the current density relative to **63**/CNT, along with approximately 10% lower FE_{CO} and reduced catalytic durability. The superior performance of the CNT-based catalyst was attributed to its higher graphitization degree, which enhances π–π interactions with **63** molecules and promotes more efficient charge transport throughout the hybrid structure.

Karthish Manthiram and collaborators explored the electrocatalytic performance of **63** immobilized on oxygen-functionalized carbon paper (**63**/OxC) in a 0.1 M $NaHCO_3$ electrolyte, with particular focus on its reactivity and mechanistic behavior.[79] The catalyst exhibited high selectivity toward CO formation, with the FE_{CO} reaching up to 96% at higher catalyst **63** loadings. As the surface loading decreased, the FE_{CO} declined moderately to approximately 80%. Notably, although the absolute current density dropped significantly at surface coverages below $\sim10^{-8}$ mol cm^{-2}, the TOF for CO production increased by several orders of magnitude. This trend highlights

Table 5 Summary of electrocatalytic CO_2 reduction to CO with catalyst **63** reported in the literature

Entry	Support/cathode	E (V)	Electrolyte	j_{CO} (mA cm^{-2})	FE_{CO} (%)	TOF (s^{-1})	Ref.
1	Carbon	−1.15 *vs.* SCE	—	0.98	87		71
2	Activated carbon fiber	−1.3 V *vs.* SEC	0.5 M $KHCO_3$	50	70		72
3	Carbon paper	−0.7 V *vs.* SCE	0.05 M K_2CO_3	1.3	86	3.5	73
4	MWCNT/carbon paper	−0.68 V *vs.* RHE	0.5 M $NaHCO_3$	13.1	92	4.08	6
5	CNT/carbon fiber paper	−0.63 V *vs.* RHE	0.1 M $KHCO_3$	10.0	92	2.7	74
6	CNT/carbon paper	−0.61 V *vs.* RHE	0.1 M $KHCO_3$	−1.0	90	2.2	75
7	CNT/carbon paper	−0.6 V *vs.* RHE	0.75 M $NaHCO_3$	−8.8	97.8	26	76
8	rGO/carbon paper	−0.6 V *vs.* RHE	0.75 M $NaHCO_3$	7.5	95.5	9.4	76
9	Acetylene black/carbon cloth	−0.7 V *vs.* RHE	0.1 M $KHCO_3$	11.6	99.8	3.9	77

a pronounced enhancement in intrinsic catalytic activity under conditions of low **63** surface density.

Cobalt phthalocyanine (catalyst **63**) is a highly promising and tunable molecular catalyst for CO_2-to-CO conversion. Its performance is strongly enhanced by immobilization on conductive carbon supports, with CNTs proving particularly effective due to superior π–π interactions and electron transfer, enabling high selectivity, current density, and operational stability.

3.3 Methanol production in H-cell

In addition to the previously reported selective generation of CO and formic acid from CO_2 electroreduction using catalyst **63**, early investigations also revealed that catalyst **63** could catalyze the conversion of CO_2 to methanol (MeOH) in an acidic solution,[80] albeit with limited FE and partial current. Subsequently, Wang and co-workers demonstrated that noncovalent immobilization of **63** onto CNTs significantly enhanced its activity for CO_2 electroreduction to MeOH. Under near-neutral conditions, this composite catalyst achieved a maximum FE_{MeOH} of 44% and j_{MeOH} of 10.6 mA cm^{-2} at an applied potential of −0.94 V *vs.* RHE (Fig. 13).[9] Further mechanistic studies by the same group provided detailed insights into the nature of the catalytically active sites and the underlying reaction pathways.[81] Spectroscopic and electrochemical analyses indicated that the molecular level dispersion of **63** on the CNT surface was crucial for achieving high activity. CO was identified as a key intermediate, whose local concentration needed to reach a critical threshold to enable further reduction to MeOH. Additionally, the bridging aza-N atoms within the *Pc* macrocycle were found to play an essential role in facilitating this transformation. Dynamic changes in the oxidation state and coordination geometry of the Co center under operating conditions were also determined to be vital for driving the multielectron CO_2-to-MeOH conversion process.

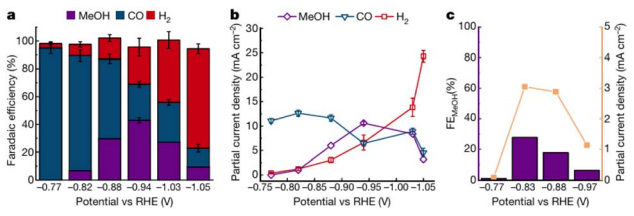

Fig. 13 Catalytic performance of catalysts **63** supported on CNTs for CO_2 and CO reduction. (a) Product selectivity, (b) partial current densities for different products *versus* electrode potential. (c) Potential dependent FE and partial current density for MeOH production from electroreduction of CO.

3.4 Transformation of second coordination sphere from homogeneous to heterogeneous electrolytic system

As outlined in Section 2.1 to 2.3, heterogeneous CO_2 electrocatalysis in a H-cell configuration utilizing immobilized molecular catalysts, including unmodified metallo-porphyrins and metallo-phthalocyanines, demonstrated exceptional catalytic performance. Specifically, metallo-porphyrins, particularly those based on iron and cobalt, were effective for converting CO_2 to CO, while cobalt phthalocyanines showed promise for producing MeOH. Copper porphyrins, on the other hand, facilitated the formation of CH_4 and C_2H_4 in aqueous electrolytes. These findings highlight the significant potential of employing molecular catalysts on electrode surfaces in aqueous and heterogeneous systems. In this section, we explore the shift from homogeneous to heterogeneous CO_2 electrocatalysis by non-covalently immobilizing molecular catalysts on the surface of electrodes. Our focus is on modifying the second coordination sphere of iron porphyrins or metal phthalocyanine, drawing inspiration from the CODH enzyme.

3.4.1 Proton source. Robert and colleagues designed a pyrene-appended iron triphenyl porphyrin featuring six pendant OH groups on the phenyl rings at all *ortho* and *ortho*′ positions (**64**, Fig. 14).[82] The molecular catalyst was immobilized onto multi-wall carbon nanotubes by drop-casting the ink onto a glassy carbon electrode. The pendant OH groups act as proton donors during the CO_2 reduction process, ensuring a high local concentration of protons due to the presence of phenolic hydroxyl substituents. The pyrene group on the modified catalyst enhances π–π interactions between the porphyrins and the carbon surface. The catalyst **64** modified electrode was tested for heterogeneous CO_2 electrocatalysis in a CO_2-saturated 0.5 M $NaHCO_3$ aqueous electrolyte at −1.03 V *vs.* NHE for 3 hours. Gas analysis of the electrolysis cell headspace revealed that the **64** modified electrode converted CO_2 to CO with a 96% faradaic efficiency, with hydrogen as a minor side product at 4%. No comparison of non-modified iron tetraphenyl porhyrins for the

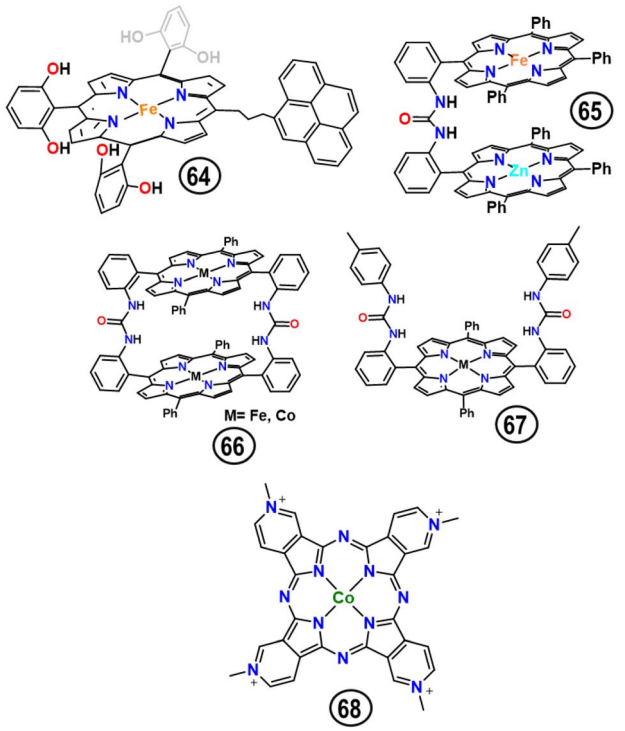

Fig. 14 Chemical structure of catalyst **64**–**68**.

heterogeneous CO_2 electrocatalysis in aqueous electrolyte was performed and reported in this work.

3.4.2 Hydrogen bond donors. In our group, we enhanced iron tetraphenyl porphyrins by decorating the second coordination sphere with urea groups (**9**), which stabilize the Fe^0–CO_2 adduct *via* multipoint hydrogen bonding, reducing overpotential while maintaining high activity and selectivity in homogeneous CO_2 electrocatalysis. Trapped water molecules in the molecular clefts proved optimal for protonation, the rate-limiting step, but the solubility of catalyst **9** decreased in DMF–water mixtures, limiting performance. To overcome this, we immobilized catalysts **9** on carbon nanotubes (CNT) for heterogeneous electrocatalysis in aqueous 0.1 M $NaHCO_3$, achieving a stable current density of -1.62 mA cm^{-2} and near 100% CO FE at -0.78 V *vs.* RHE.[83] Control experiments with unmodified **1**/CNT showed significantly lower activity (76% FE), confirming the critical role of urea-derived hydrogen bonds in enhancing CO_2 reduction, successfully transitioning second-sphere effects from homogeneous to heterogeneous systems.

3.4.3 Bimetallic system. The bimetallic approach modifies iron porphyrins by introducing a second metal center, inspired by [NiFe]-CODH's synergistic electron storage and CO_2 activation. While homogeneous CO_2 electrocatalysis in DMF showed no improvement due to protonation bottlenecks, heterogenizing Fe–Fe (**21**) and Fe–Zn (**65**) catalysts on CNTs shifted the rate-determining step. In aqueous CO_2 reduction, catalyst **21** achieved a fourfold current density increase and ac. 90% CO faradaic efficiency, outperforming catalyst **1** (<80%). Surprisingly, catalyst **65** also enhanced performance, confirming bimetallic cooperativity, not Zn activity, drives the improvement.

This work highlights how bimetallic second-sphere interactions boost heterogeneous eCO_2-to-CO conversion in water. Overcoming protonation limitations *via* heterogenization unlocked cooperative effects, with Fe–Fe and Fe–Zn complexes both enhancing catalytic activity and selectivity beyond monometallic systems. The results underscore the potential of bimetallic design for efficient electrocatalysis in aqueous environments.

Cao *et al.* recently reported a double urea-bridged, box-like dinuclear porphyrin catalyst, **66** (with Co or Fe centers, Fig. 14), drop-cast on CNT for heterogeneous CO_2RR in aqueous $KHCO_3$.[84] It achieved high FE CO (>96.3% for Co, >93.8% for Fe) at lower overpotentials (~180 mV for Co, ~230 mV for Fe) and showed a four times increase in TON/TOF over mononuclear analogs (catalyst **67**). The enhanced performance is attributed to the cavity stabilizing CO_2 adducts and facilitating proton delivery.

3.4.4 Electrostatic environment. Robert and co-workers enhanced the catalytic activity of catalyst **34** by replacing *para*-phenyl hydrogen with positively charged trimethylanilinium groups. These modifications created coulombic interactions with the negatively charged Fe^0–CO_2 adduct, significantly reducing the overpotential for CO_2 electrocatalysis in water. The water-soluble catalyst was then immobilized on carbon paper *via* spray-coating with carbon powder and Nafion, which prevented leaching while ensuring uniform distribution. In CO_2-saturated 0.1 M KCl/0.5 M $KHCO_3$ electrolyte at -0.96 V *vs.* SHE, the modified electrode maintained ~90% FE CO and 1 mA cm^{-2} current density over 30 hours.[85] In contrast, unmodified catalyst **1** rapidly degraded under the same conditions. This work successfully translated second-sphere electrostatic effects from homogeneous to heterogeneous systems, demonstrating stable and efficient CO_2-to-CO conversion.

Inspired by [NiFe]-CODH, our research group incorporated pyridinium groups into cobalt(II) tetrapyridinoporphyrazine (**68**, Fig. 14) to enhance CO_2-to-methanol conversion.[86] While homogeneous testing in water was hindered by adsorption issues, heterogenization *via* electrodeposition on CNTs enabled efficient catalysis, achieving 15% FE for methanol – more than double the 7% efficiency of unmodified catalyst **63**. Remarkably, while CO electrolysis with **63** confirmed CO as a methanol intermediate (6.9% to 4% efficiency), catalyst **68** showed negligible methanol formation from CO, suggesting a distinct CO-free pathway. This demonstrates how second-sphere modifications can fundamentally alter reaction mechanisms.

The pyridinium environment not only tripled the methanol current density compared to catalyst **63** but also appeared to bypass the conventional CO intermediate, highlighting the critical role of cationic groups in both enhancing activity and redirecting reaction pathways. These findings open new possibilities for designing molecular catalysts that can steer multi-electron CO_2 reduction toward specific products, though further *in situ* studies are needed to fully elucidate the underlying mechanism. The work provides a clear example of how

strategic ligand design can simultaneously boost efficiency and control selectivity in electrochemical CO_2 electrocatalysis.

Inspired by the [NiFe]-CODH enzyme, molecular catalysts designed with tailored second coordination spheres have been successfully adapted from homogeneous to heterogeneous CO_2 electrolysis. Key modifications, including proton donors, hydrogen-bond networks, bimetallic cooperativity, and engineered electrostatic environments, have been effectively translated to electrode surfaces through non-covalent immobilization. This shift not only enhances catalytic activity, selectivity, and stability in aqueous systems but also advances the practical applicability of molecular catalysts, bridging the gap between precise molecular design and real-world electrolyzer performance.

3.5 Molecules for heterogeneous catalysis on flow-cell configuration

Although the reported FE% for the molecule catalysts in batch cells, including H-type cell, achieved very high values near to 99% for CO_2 reduction,[87] the current densities were limited in the range of 0.1–35 mA cm^{-2}. It promotes the researchers moving to the application of flow cell configuration to increase the current density of CO_2 electroreduction by accommodating the mass-transport limitations of the batch type. The electrolyte flow rate is higher to reduce the diffusion layer thickness from typical 50 μm to 50 nm,[88] and the CO_2 gas can be directly supplied to the reaction interface. Therefore the local chemical microenvironment of the catalyst changes in a positive way, which promote the CO_2 production rate.[89] The flow cell is therefore employed as a platform for the test which targets scaling-up and long-term stability tests. A pronounced demonstration target is more than 20k hours at >200 mA cm^{-2} in order for an economical production.[88] A typical work from Ren *et al.*[90] showed that the current density could be 150 mA cm^{-2} at the FE of 95% for CO_2 to CO conversion with cobalt phthalocyanine catalyst in zero-gap flow cell. Table S1 shows the typical performance of the molecular catalysts on flow-cell configuration. It would not be surprising that the current density keeps at a high level with the flow cell. However, it should be noted that durability becomes one of the optimization targets when we move to flow-cell electrolysis, and more critical technical parameters pop out in such a study. With them the stability of the catalyst immobilized gas diffusion electrode should be awarded in the study. The first potential degradation issue on stability is the loss of catalyst loading. It can be detachment or leaching. Li *et al.* found that although there was no structural damage to the molecular catalyst, the product selectivity decreases potentially because of the detachment of the **1** molecules on the Cu substrate.[91] It was found the current densities for catalyst **69** and **70** (Fig. 15) decreased by 20–30% after 30 min in the electrolysis at −0.62 V *vs.* RHE. Su *et al.*[92] suggested it was due to the leaching of the catalyst with soluble amino and trimethylamine group in aqueous solution. Immobilization of the molecular catalysts on CNT was proposed as a potential solution to against leaching. It was proposed that fixing the metal phthalocyanine or porphyrin on the substrate

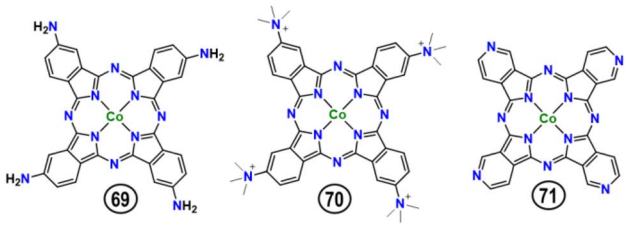

Fig. 15 Chemical structure of catalyst **69**, **70** and **71**.

in axial coordination way could improve the stability of the catalyst in electrolysis. It can be realized by functionalizing the substrate with amino. The formation of Co–N axial coordination lowered the reduction potential of **60**, therefore stabilized the catalyst and realized a stable operation for 100 h.[93]

As for a flow cell system, high energy efficiency and productivity are targeted as the major targets for process optimization. Most of the studies does not provide the energy efficiency value, but it can be estimated from the typical overpotential and the corresponding partial current density for the desired CO_2 reduction products:[87]

$$EE_{cathode}\ (\%) = \Delta P_0/\Delta P \times FE\% \quad (1)$$

where the $EE_{cathode}$ is the cathodic energy efficiency in this equation, ΔP_0 is the equilibrium cathodic potential, which is −0.11 V *vs.* reversible hydrogen electrode (RHE) for CO production from CO_2 at room temperature at 1 bar, ΔP is the overpotential in electrolysis, FE% is the faradaic efficiency at this overpotential. A typical reported value for $EE_{cathode}$ is 23% for **1**/Cu sputtered PTFE GDE in a flow cell for ethanol production.[91] Most of the flow cell test prefer to provide the electrolysis cell energy efficiency, EE, which also include the contribution from the ion exchange membrane and anodic reaction. Typically, the EE of a CO_2 flow cell was less than 40% during the long term operation.[94] With the addition of potassium triflate (KOtf) as an additive to provide K^+ cations to the substrate with catalyst **71** (Fig. 15), EE can be elevated to 60.7–76.4%. It is understandable to perform the cell as a whole system, and it is also well-known the membrane and anodic reaction has influence on the cathodic reaction. The application of different types of membrane would have effect on the product and carbonate ion crossover between the anolyte and catholyte, which changes the catholyte composition and further alter the electrolysis performance.[95] Heβelmann *et al.*[96] estimated the obvious influence of the ion exchange membrane on the CO_2 electrolyzer performance in the scenario of CO and syngas production (Fig. 16). The type of membrane can also modify the local pH environment of the cathodic catalyst so that the major proton source can be different for the cathodic reaction[97] and the strategy of facilitating CO_2 electroreduction will be different. Moreover, it should be noted that the parameters of the membrane, such as the thickness also matters in the optimization of flow cell performance.[98] Furthermore, the re-oxidation of the crossover products in the anolyte has been proven to have influence on the FE and then the EE.[99] There are suggestions for

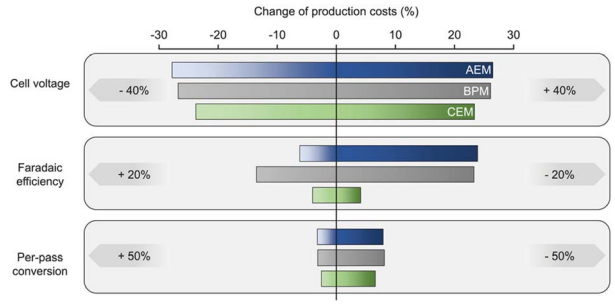

Fig. 16 Sensitivity of the different membrane in CO_2 electrolyzer for CO production towards a change in performance.[96]

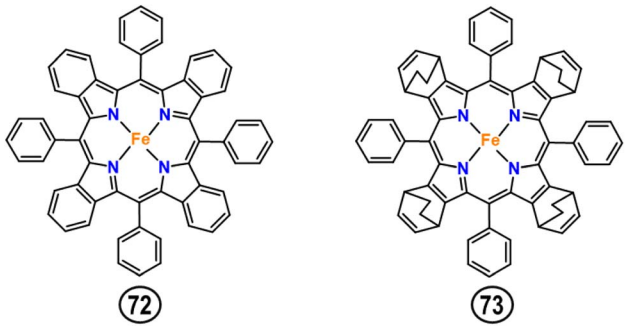

Fig. 17 Chemical structure of **72** and **73**.

the collection of the anolyte sample but the study to increase the oxidation overpotential of the CO_2 products on the anode catalyst is also necessary.

Besides the performance evaluation for the flow cell development, due to the relatively high production cost for molecule catalysts, the loading amount of the catalyst on the gas diffusion electrode is also important from the economic viewpoint. Although the loading amount of catalyst is also massively contributed by the catalyst itself and the immobilization method of the catalyst on the electrode which were discussed in the previous sections, optimization of the flow cell system design could help to reduce the loading amount furthermore. For instance, the flow channel design of the electrode flow field plate has effect on the distribution of feedstock and gas product. Ideally, a uniform CO_2 and H_2O distribution within the cell benefits the full-utilization of the catalyst. However, considering the potential large gradiences of pH value of the aqueous solution and CO/CO_2 concentrations form the inlet to outlet with commercial-relevant current densities, an engineering effort with the help of multi-field optimization from case to case will become increasing important for high TRL development. Moreover, gas diffusion electrode microstructure design alters the triple-phase boundary length for the proton coupled electron transfer reactions. A well design of the pore distribution, catalyst dispersion map, water transport properties, and electrical conductivity of the electrode would increase the current density of the reaction by efficient creating electrochemical reaction sites inside.

3.6 The co-catalysts of molecules and nanoparticles

Recently, increasing efforts have been made to integrate molecular catalysts with metallic catalysts to enhance catalytic performance in tandem processes, particularly for CO_2 electrocatalysis beyond the two-electron, two-proton pathway to CO. Molecular components offer greater versatility than metals due to their tunable electronic and structural properties through synthetic modifications. This makes them more promising for CO_2 electrolysis toward C_{2+} products or beyond CO compared to bimetallic catalysts.

Buonsanti and co-works engineered a series of iron porphyrin catalysts with tunable π-delocalization for CO_2 electrolysis (Fig. 17). Catalyst **72** emerged as the top performer, achieving 91% FE for CO production in aqueous electrolyte, outperforming both the less delocalized catalyst **1** and the more σ-donating catalyst **73**.[11] This performance hierarchy (TOF_{CO}: **72** > **1** > **73**) directly correlated with the degree of aromatic delocalization in the molecular structures.

The researchers then paired these porphyrins with CO_2-to-C_{2+} active Cu nanocubes (Cu_{cub}) to create tandem systems. The Cu_{cub}/**72** combination proved most effective, delivering a remarkable 22-fold enhancement in ethylene selectivity (36% at −1.05 V *vs.* RHE) along with a 100 mV positive shift in onset potential compared to bare Cu_{cub}. These results highlight how molecular catalyst design can dramatically improve both the efficiency and selectivity of CO_2 conversion in hybrid catalytic systems (Fig. 18).

The same research team also combined cobalt phthalocyanine (**63**) with Cu nanocubes (Cu_{cub}) on carbon electrodes for CO_2 electrolysis. Using only **63** yielded CO with 95% efficiency, while Cu_{cub} alone produced mixed products (CO, C_{2+}, H_2).[100] The hybrid **63**-Cu_{cub}/C system suppressed H_2 evolution and boosted C_{2+} selectivity to 48% (Fig. 19), demonstrating enhanced C–C coupling when molecular and nanocatalysts were closely integrated. Key findings revealed that spatial proximity between **63** and Cu_{cub} was crucial, the molecular

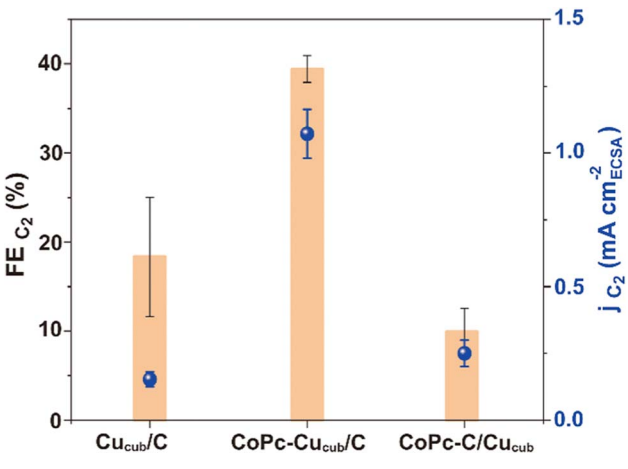

Fig. 18 FE of C_2 products and C_2 partial current density (j_{C_2}) *vs.* different electrodes normalized by the ECSA. The figure has been reconstructed from the ref. 100.

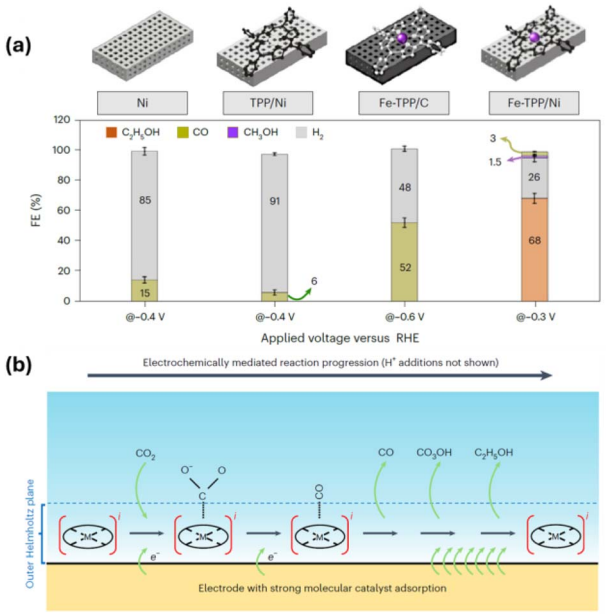

Fig. 19 (a) FE of TPP and **1**/Ni at their optimal potential of −0.3 V; bare nickel at the optimal potential of −0.4 V; and **1**/C at the optimal potential of −0.6 V *versus* RHE, (b) schematic representation of an electrochemical reaction mechanism in which a molecular catalyst resides inside the electric double layer. Here electron transfers from the electrode occur during the CO_2 reduction reaction, preventing substantial oxidation of the hybrid organometallic catalyst or its metal centre.

catalyst's high CO output near Cu sites promoted C_{2+} formation. This tandem approach optimized both CO generation (from **63**) and coupling (on Cu_{cub}), offering a strategic path for efficient multi-carbon synthesis from CO_2.

Moreover, Burdyny and the coll., achieved a breakthrough by immobilizing catalyst **1** on 3D nickel electrodes, creating a hybrid system that converts CO_2 to ethanol with 68% FE, far surpassing the performance of Ni foam alone (15% CO, Fig. 20) or carbon-supported **1** (52% CO).[101] The unique **1**/Ni configuration achieves exceptional performance through direct electronic coupling that stabilizes the iron center's oxidation state while enabling multi-carbon product formation (68% ethanol, 3% CO, and 1.5% methanol). Unlike control systems that primarily produce CO, this hybrid catalyst completely shifts the product spectrum toward ethanol selectivity, demonstrating how tailored metal-molecular interactions can redirect catalytic pathways. The exceptional performance arises from synergistic Ni–Fe interactions that fundamentally alter the molecular catalyst's behavior. The nickel substrate not only suppresses CO release by inhibiting Fe^{I} formation but also weakens *CO binding when iron exists in its Fe^{II}/Fe^{III} states, thereby driving the reaction pathway toward ethanol production. This work provides concrete evidence that strategic integration of molecular catalysts with metal electrodes can unlock new reaction pathways, transforming CO_2 electroreduction from C_1 to valuable C_2 products through carefully engineered electronic interactions at the hybrid interface.

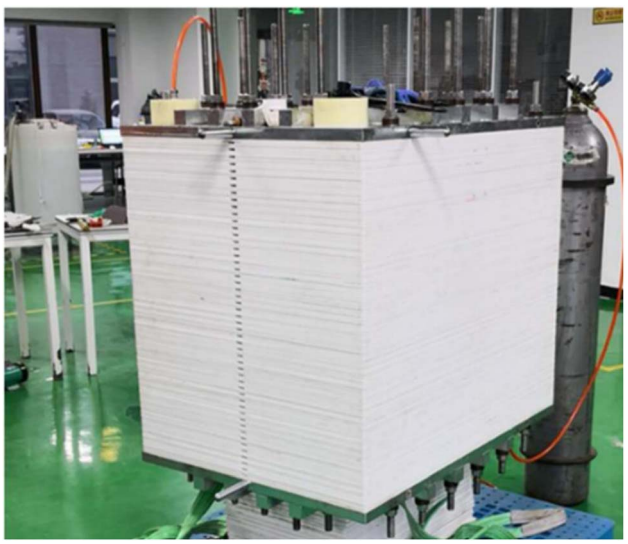

Fig. 20 Pilot scale CO_2 electrolyzer developed by Kang's group.[2] Copyright licensed by ACS 2025.

3.7 Industrial requirements for molecular catalysts

These findings underscore how tailored integration of molecular and metallic catalysts can unlock new mechanistic pathways, offering a versatile platform to control product distributions in CO_2 electroreduction. As research progresses, such co-catalyst systems hold significant promise for scaling sustainable electrochemical CO_2 conversion to multi-carbon fuels and chemicals.

From a technoeconomic perspective, the feasibility of electrochemical CO_2 conversion is affected by many factors, within which the product spectrum significantly decides the production cost. Production of CO from CO_2 electrolysis is believed to be one of the most commercially feasible processes[102] with fulfilling the preset performance requirements. Segets *et al.*[103] proposed the minimum requirements for industrial applications. The ones closely related to catalyst performance are: (1) current density higher than 0.2 A cm^{-2}. (2) FE is higher than 80%. (3) Cell voltage lower than 3.0 V and ideally lower than 2.0 V. (4) Stability of 50 000 h with a voltage decay rate of <0.01 mV h^{-1} and FE% decrease <0.1% per 1000 h. Most of the above performance requirements can be achieved based on the lab data (Table S1), except that the stability test needs to be processed with longer time under industrial conditions. Meanwhile, it should be noted that lab data is critically different from industrial plant performance data. The latter could be much lower than the lab data due to the poor stack design and other phenomena such as pressure drop, current distribution throughout the electrode, inefficient flow field. (5) Single pass conversion higher than 50%, which was rarely reported for molecular catalysts but is a key parameter for the design of stack system. (6) Robustness against industrial gas impurities and low concentration of CO_2. Depending on the CO_2 sources, the concentration of CO_2 varies from 1 to 44% in industrial gas emission. Meanwhile, O_2, CO, SO_2, NO_x, H_2, CH_4,

and HCl may present in the gas sources.[104] Although most of the impurities can be removed before the CO_2 electrolyzer, the performance of molecular catalyst equipped CO_2 electrolyzer still needs careful evaluation, which researchers have already paid attention to with the present of traces of O_2, NO_2 and SO_2.[105–107]

Commercialization does not only require performance as the key performance indicators (KPIs) but also cost and scale, which has been summarized in the recent work by García de Arquer.[108] The cost of catalyst is included inside the stack investment cost and MEA replacement cost.[109] The loading amount and production cost contribute to both parts. Considering the loading of noble metals in water electrolyzer varies from 0.05 to 2 mg cm^{-2} (ref. 110) with a price of around 300–4000 euro per g,[111] the loading of molecular catalysts falls within a potential affordable range (for instance, FeTPP is around €380 per gram).[112] Meanwhile, the production scale of catalyst materials should match the commercial electrolysis production needs. A 25 kW CO_2 electrolyzer has been developed by Siemens and Evonik.[113] Kang's group reported a pilot scale CO_2 electrolyzer with net 30 t per a CO_2 conversion capacity to produce syngas.[2] The authors are not aware of any application of molecular catalysts in these pilot plant tests. The CO_2-to-CO electrolysis plant needs to reach a capacity of 96 N m^3 h^{-1} of CO as a benchmark.[108]

4 Conclusions and perspective

In this contribution, we review various bio-inspired strategies that chemists are employing to design new molecular catalysts for CO_2RR. We focus specifically on iron porphyrins and cobalt phthalocyanines, which remain among the most efficient molecular catalysts developed to date. Drawing inspiration from enzymatic systems that activate small molecules, we examine how these biological principles are being translated into discrete synthetic molecular systems. Through this analysis, we offer an updated perspective on the progress made toward designing more effective molecular catalysts. To structure our discussion, we categorize these bio-inspired functions into the following key areas:

(i) Hydrogen bonding, (ii) bimetallic cooperativity, (iii) local proton sources, (iv) electrostatic interactions, (v) entatic states and (vi) structural dynamics. Although it remains premature to draw definitive conclusions about the individual impact of these chemical functionalities on catalytic enhancement relative to the parent iron porphyrins or cobalt phthalocyanines, some tentative insights can be gleaned from current strategies. Notably, the introduction of hydrogen-bonding functionalities, whether single or multiple points, has significantly improved both the kinetics and thermodynamics of CO_2RR. These hydrogen-bonding motifs, acting as either donors or acceptors, contribute to the stabilization of metal-bound CO_2 intermediates, thereby enabling enhanced catalytic reactivity. Further work should focus on optimizing the positioning of hydrogen bonds to promote CO_2 activation by strengthening HB interactions with the activated CO_2 molecule. Examination of the CODH active site indicates that the amino acid residues forming hydrogen bonds with bound CO_2 are more suitably positioned above the activated CO_2, rather than laterally, as observed in most synthetic mimics. It is also anticipated that the nature of the functional groups responsible for hydrogen bonding with bound CO_2 will be crucial for enhancing both interaction strength and the degree of CO_2 activation. Furthermore, stabilization of the Fe–CO intermediate through an appropriate hydrogen-bonding network involving well-chosen HB donors may facilitate further reduction of CO_2 to more reduced products such as CH_3OH or CH_4. Therefore, mastering molecular engineering strategies that precisely position hydrogen-bonding functionalities in molecular-based catalysts remains a key challenge for chemists.

The presence of confined water molecules between the metal-bound CO_2 and nearby hydrogen-bonding functionalities has been shown to influence chemical reactivity, in some cases steering the reaction pathway toward the direct reduction of CO to methanol. However, further studies are required to gain deeper insight into the chemical nature and specific roles of these water molecules, particularly how they are stabilized through hydrogen bonding in proximity to the activated CO_2 intermediate or their role in the convoy of protons. The development of multimetallic molecular catalysts that distribute the roles of redox activity and Lewis acidity has led to notable improvements in CO_2 reduction catalysis. In particular, bimetallic systems such as iron porphyrins have demonstrated enhanced performance. However, several questions remain unresolved. For example, in the reduced Fe(I)–Fe(0) state of bimetallic iron porphyrins, it has been proposed that the Fe(I) center may act as a Lewis acid. Additionally, the presence of two redox-active centers raises the question of why more than two electrons are not transferred to the CO_2 molecule during catalysis in a scenario where CO_2 lies in between the two redox active metal centers. Understanding the limitations in electron transfer and the precise mechanistic roles of each metal center remains an open area of investigation. Facilitating rapid proton delivery to the active site during the CO_2RR has resulted in significant improvements in both overpotential and turnover frequency of molecular catalysts. To date, phenol groups have been the most extensively studied for this purpose. However, the development of alternative functional groups as potential proton donors remains an area with untapped synthetic opportunities. One of the most significant advances in the design of molecular catalysts for CO_2RR has been the incorporation of chemical functionalities that enable electrostatic interactions with charged intermediates or transition states. The attachment of various cationic groups to catalyst frameworks has led to notable improvements in CO_2RR activity. However, the fundamental role and mechanistic implications of these electrostatic interactions remain to be fully understood. For example, the aquation of cationic groups has been suggested to divert the reaction pathway toward the hydrogen evolution reaction (HER). Meanwhile, DFT studies suggest that flexible cationic moieties can generate a shielding effect against solvent molecules, thereby facilitating CO_2 access to the active site. Further experimental and computational investigations are needed to clarify these competing effects. Of note, the presence

of redox-active cationic fragments, such as imidazolium or pyridinium units, may also interfere with the catalytic activity of the metal complex.[114] The enforcement of specific geometric constraints in molecular complexes, commonly observed in biological systems, remains an area with significant potential for advancement in synthetic catalyst design. However, maintaining such constrained geometries in small synthetic systems poses a considerable challenge, as these structures often tend to relax into more thermodynamically stable, but less active, conformations. Shifting away from a static view of the active form of molecular catalysts is an emerging and actively investigated area. Notably, Shaw and colleagues have been exploring how core flexibility within molecular catalysts can influence their reactivity profiles. Incorporating such dynamic features into synthetic systems remains a significant challenge but holds promise for providing a more nuanced and realistic understanding of molecular catalysis, one that better reflects the adaptable behavior often observed in enzymatic systems.[115] In summary, it is anticipated that a thoughtful integration of the various factors discussed—ranging from hydrogen bonding and electrostatic interactions to geometric constraints and structural dynamics—will be key to achieving catalytic activities that begin to rival those of enzymatic systems. However, the ultimate goal may not lie in merely summing these individual effects, but rather in uncovering new, yet unexplored, dimensions of molecular catalysis that emerge from their interplay. One of the major challenges in CO_2 chemistry is the direct capture and conversion of CO_2 at low concentrations (~420 ppm in air). In a recent study, Rui Cao and co-workers reported that the addition of triethanolamine (TEOA) in the presence of FeTPP and CO_2 in an organic medium, leads to a dramatic increase in the catalytic current for CO_2-to-CO conversion.[116] Through combined experimental and theoretical investigations, the authors attributed this remarkable enhancement to the ability of TEOA to capture CO_2 and shuttle the activated CO_2 species to the active Fe(0)TPP site, where it is subsequently released. Although no systematic investigation of the CO_2 concentration was carried out in this study, it nonetheless provides a clear example of how CO_2 capture can enable its utilization at low concentrations when directly coupled to catalytic conversion. However, the identity of the species actually undergoing reduction, whether the zwitterionic alkylcarbonate intermediate or the subsequently released free CO_2, remains to be fully elucidated. In this area of research, much effort needs to be dedicated to perform CO_2 reduction at low concentration. Another grand challenge concerns the reduction of CO_2 in the presence of O_2. As a much stronger oxidant, O_2 competes with CO_2 reduction, which occurs at significantly more negative potentials than O_2 reduction. Moreover, partially reduced oxygen species can also interfere with the process and prove deleterious to molecular catalysts. We believe that this topic warrants a dedicated review of its own and therefore lies beyond the scope of the present review.

The application of bio-inspired strategies to molecular catalysts such as metalloporphyrins and metallophthalocyanines has demonstrably improved their performance in the homogeneous CO_2RR, effectively reducing overpotentials and accelerating reaction rates. Despite this progress, the working mechanisms of these bio-strategies remain inadequately elucidated.

In pursuit of scalable CO_2 electrolysis, research over the past two decades has focused on transitioning these molecular catalysts to heterogeneous configurations. By immobilizing them on electrodes within aqueous electrochemical cells, researchers have maintained high catalytic reactivity for a range of products, from CO to methanol, while reducing catalyst mass requirements by orders of magnitude. The incorporation of bio-inspired functional groups remains effective in these heterogeneous systems, yet a significant knowledge gap persists regarding the surface-level mechanisms. Detailed mechanistic studies are imperative to inform the rational design of advanced catalysts capable of meeting industrial benchmarks. Concurrently, the development of molecular-metallic co-catalyst systems shows promise for achieving multi-carbon (C_{2+}) products, though their synergistic mechanisms are similarly unexplored.

For future catalysts to be industrially viable, they must meet stringent criteria including high current density (>0.2 A cm^{-2}) and FE (>80%), low cell voltage (<3.0 V, ideally <2 V), exceptional long-term stability (>50 000 h), high single-pass conversion (>50%), and robustness against gas impurities (O_2, SO_2, NO_x, *etc.*). While laboratory results are promising, translating these findings into practical, industrial-scale applications, particularly in terms of stability and performance under complex gas feed conditions, remains a key challenge for the research community.

Author contributions

Aakash Santra and Arnab Ghatak wrote the homogeneous CO_2RR part, wrote the first draft, involved in drawing and overall development of the manuscript. Zhiyuan Chen, Jing Shen, Joost Helsen, and Yuvraj Birdja wrote the heterogeneous CO_2RR part. Ally Aukauloo, and Chanjuan Zhang supervised the whole work.

Conflicts of interest

There are no conflicts to declare.

Data availability

The data supporting this article have been included as part of the supplementary information (SI). Supplementary information is available. See DOI: https://doi.org/10.1039/d5sc07983g.

Acknowledgements

The authors acknowledge the support from the European Union's Horizon 2020 research and innovation programme under grant agreement no. 101037389 (ECO2FUEL) and Flanders Innovation & Entrepreneurship (VLAIO) under project no. HBC.2023.0565 (ELCO2SYN). The work was also supported by the T-REX project funded by the federal Energy Transition Fund

(ETF) by FPS Economy, Belgium. This work was supported by the Université Paris-Saclay, CNRS and the French National Agency for Research within the France 2030 plan (Air Capture, ANR-24-RRII-0004). A. A. thanks the Institut Universitaire de France for support.

Notes and references

1 C. Zhang, P. Gotico, R. Guillot, D. Dragoe, W. Leibl, Z. Halime and A. Aukauloo, *Angew. Chem., Int. Ed.*, 2023, **62**, e202214665.
2 Y. Cheng, P. Hou, X. Wang and P. Kang, *Acc. Chem. Res.*, 2022, **55**, 231–240.
3 H.-P. Iglesias van Montfort, S. Subramanian, E. Irtem, M. Sassenburg, M. Li, J. Kok, J. Middelkoop and T. Burdyny, *ACS Energy Lett.*, 2023, **8**, 4156–4161.
4 Y.-J. Ko, C. Lim, J. Jin, M. G. Kim, J. Y. Lee, T.-Y. Seong, K.-Y. Lee, B. K. Min, J.-Y. Choi, T. Noh, G. W. Hwang, W. H. Lee and H.-S. Oh, *Nat. Commun.*, 2024, **15**, 3356.
5 C. Costentin, S. Drouet, M. Robert and J.-M. Savéant, *Science*, 2012, **338**, 90–94.
6 M. Wang, K. Torbensen, D. Salvatore, S. Ren, D. Joulié, F. Dumoulin, D. Mendoza, B. Lassalle-Kaiser, U. Işci, C. P. Berlinguette and M. Robert, *Nat. Commun.*, 2019, **10**, 3602.
7 S. Yang, Y. Sun, C. Wang, L. Lv, M. Hu, J. Jin and H. Xie, *Catal. Sci. Technol.*, 2023, **13**, 758–766.
8 G. Zhang, T. Wang, M. Zhang, L. Li, D. Cheng, S. Zhen, Y. Wang, J. Qin, Z.-J. Zhao and J. Gong, *Nat. Commun.*, 2022, **13**, 7768.
9 Y. Wu, Z. Jiang, X. Lu, Y. Liang and H. Wang, *Nature*, 2019, **575**, 639–642.
10 X. Gao, Y. Jiang, J. Liu, G. Shi, C. Yang, Q. Xu, Y. Yun, Y. Shen, M. Chang, C. Zhu, T. Lu, Y. Wang, G. Du, S. Li, S. Dai and L. Zhang, *Nat. Commun.*, 2024, **15**, 10331.
11 M. Wang, V. Nikolaou, A. Loiudice, I. D. Sharp, A. Llobet and R. Buonsanti, *Chem. Sci.*, 2022, **13**, 12673–12680.
12 Y. Lum, B. Yue, P. Lobaccaro, A. T. Bell and J. W. Ager, *J. Phys. Chem. C*, 2017, **121**, 14191–14203.
13 A. J. Fielding, E. G. Kovaleva, E. R. Farquhar, J. D. Lipscomb and L. Que Jr, *JBIC, J. Biol. Inorg. Chem.*, 2011, **16**, 341–355.
14 J. P. Emerson, E. G. Kovaleva, E. R. Farquhar, J. D. Lipscomb and L. Que Jr, *Proc. Natl. Acad. Sci. U. S. A.*, 2008, **105**, 7347–7352.
15 G. Xue, A. T. Fiedler, M. Martinho, E. Munck and L. Que Jr, *Proc. Natl. Acad. Sci. U. S. A.*, 2008, **105**, 20615–20620.
16 A. Khadhraoui, P. Gotico, B. Boitrel, W. Leibl, Z. Halime and A. Aukauloo, *Chem. Commun.*, 2018, **54**, 11630–11633.
17 C. Costentin, M. Robert and J.-M. Savéant, *Chem. Soc. Rev.*, 2013, **42**, 2423–2436.
18 P. Gotico, Z. Halime and A. Aukauloo, *Dalton Trans.*, 2020, **49**, 2381–2396.
19 J. P. Collman, M. Rapta, M. Bröring, L. Raptova, R. Schwenninger, B. Boitrel, L. Fu and M. L'Her, *J. Am. Chem. Soc.*, 1999, **121**, 1387–1388.
20 J. P. Collman, R. Boulatov, C. J. Sunderland and L. Fu, *Chem. Rev.*, 2004, **104**, 561–588.
21 J. P. Collman, N. K. Devaraj, R. A. Decréau, Y. Yang, Y.-L. Yan, W. Ebina, T. A. Eberspacher and C. E. D. Chidsey, *Science*, 2007, **315**, 1565–1568.
22 P. Sen, B. Mondal, D. Saha, A. Rana and A. Dey, *Dalton Trans.*, 2019, **48**, 5965–5977.
23 E. M. Nichols, J. S. Derrick, S. K. Nistanaki, P. T. Smith and C. J. Chang, *Chem. Sci.*, 2018, **9**, 2952–2960.
24 S. R. Ahrenholtz, C. C. Epley and A. J. Morris, *J. Am. Chem. Soc.*, 2014, **136**, 2464–2472.
25 S. Samanta, K. Sengupta, K. Mittra, S. Bandyopadhyay and A. Dey, *Chem. Commun.*, 2012, **48**, 7631–7633.
26 C. Costentin and J.-M. Savéant, *J. Am. Chem. Soc.*, 2017, **139**, 8245–8250.
27 S. Amanullah, P. Gotico, M. Sircoglou, W. Leibl, M. J. Llansola-Portoles, T. Tibiletti, A. Quaranta, Z. Halime and A. Aukauloo, *Angew. Chem., Int. Ed.*, 2024, **63**, e202314439.
28 P. Gotico, B. Boitrel, R. Guillot, M. Sircoglou, A. Quaranta, Z. Halime, W. Leibl and A. Aukauloo, *Angew. Chem., Int. Ed.*, 2019, **58**, 4504–4509.
29 S. Patra, S. Bhunia, S. Ghosh and A. Dey, *ACS Catal.*, 2024, **14**, 7299–7307.
30 S. Patra, S. Ghosh, S. Samanta, A. Nayek and A. Dey, *J. Organomet. Chem.*, 2025, **1023**, 123439.
31 M. Hammouche, D. Lexa, M. Momenteau and J. M. Saveant, *J. Am. Chem. Soc.*, 1991, **113**, 8455–8466.
32 O. Enoki, T. Imaoka and K. Yamamoto, *Macromol. Symp.*, 2003, **204**, 151–158.
33 Y. Yao, J.-H. Wu, G. Liu, R. Zhang, Z.-S. Yang, S. Gao, T.-C. Lau and J.-L. Zhang, *ChemCatChem*, 2024, **16**, e202301705.
34 E. A. Mohamed, Z. N. Zahran and Y. Naruta, *Chem. Commun.*, 2015, **51**, 16900–16903.
35 P. Gotico, Z. Halime, W. Leibl and A. Aukauloo, *ChemPlusChem*, 2023, **88**, e202300222.
36 Z. N. Zahran, E. A. Mohamed and Y. Naruta, *Sci. Rep.*, 2016, **6**, 24533.
37 E. A. Mohamed, Z. N. Zahran and Y. Naruta, *J. Mater. Chem. A*, 2021, **9**, 18213–18221.
38 L. K. Frensch, K. Pröpper, M. John, S. Demeshko, C. Brückner and F. Meyer, *Angew. Chem., Int. Ed.*, 2011, **50**, 1420–1424.
39 G. Kour, X. Mao and A. Du, *ChemNanoMat*, 2021, **7**, 935–941.
40 M. Haake, B. Reuillard, M. Chavarot-Kerlidou, C. Costentin and V. Artero, *Angew. Chem., Int. Ed.*, 2024, **63**, e202413910.
41 S. Sinha and J. J. Warren, *Inorg. Chem.*, 2018, **57**, 12650–12656.
42 C. Costentin, G. Passard, M. Robert and J.-M. Savéant, *Proc. Natl. Acad. Sci. U. S. A.*, 2014, **111**, 14990–14994.
43 C. G. Margarit, C. Schnedermann, N. G. Asimow and D. G. Nocera, *Organometallics*, 2019, **38**, 1219–1223.
44 K. Kosugi, M. Imai, M. Kondo and S. Masaoka, *Chem. Lett.*, 2022, **51**, 224–226.
45 A. Sonea and J. J. Warren, *ACS Catal.*, 2025, **15**, 1444–1454.
46 I. Azcarate, C. Costentin, M. Robert and J.-M. Savéant, *J. Am. Chem. Soc.*, 2016, **138**, 16639–16644.

47 C. Costentin and J.-M. Savéant, *Nat. Rev. Chem.*, 2017, **1**, 0087.
48 C. G. Margarit, N. G. Asimow, M. I. Gonzalez and D. G. Nocera, *J. Phys. Chem. Lett.*, 2020, **11**, 1890–1895.
49 A. Khadhraoui, P. Gotico, W. Leibl, Z. Halime and A. Aukauloo, *ChemSusChem*, 2021, **14**, 1308–1315.
50 K. Guo, X. Li, H. Lei, H. Guo, X. Jin, X.-P. Zhang, W. Zhang, U.-P. Apfel and R. Cao, *Angew. Chem., Int. Ed.*, 2022, **61**, e202209602.
51 M. R. Narouz, P. De La Torre, L. An and C. J. Chang, *Angew. Chem., Int. Ed.*, 2022, **61**, e202207666.
52 S. Ghosh, S. Patra, A. Bisoi, S. Ghosh, N. Maurya, A. Das, P. C. Singh and A. Dey, *ACS Catal.*, 2025, **15**, 3595–3610.
53 S. E. Lawson, R. J. Roberts, D. B. Leznoff and J. J. Warren, *J. Am. Chem. Soc.*, 2024, **146**, 22306–22317.
54 A. Smith, P. Gotico, R. Guillot, S. Le Gac, W. Leibl, A. Aukauloo, B. Boitrel, M. Sircoglou and Z. Halime, *Adv. Sci.*, 2025, **12**, 2500482.
55 H. He, Z.-Y. Qiu, Z. Yin, J. Kong, J.-S. Dang, H. Lei, W. Zhang and R. Cao, *Chem. Commun.*, 2024, **60**, 5916–5919.
56 S. Patra, S. Dinda, S. Ghosh, T. Roy and A. Dey, *Proc. Natl. Acad. Sci. U. S. A.*, 2025, **122**, e2417764122.
57 Y. Pan, W. Chen, S. Lu and Y. Zhang, *Dyes Pigm.*, 2005, **66**, 115–121.
58 T. A. Fassbach, J.-M. Ji, A. J. Vorholt and W. Leitner, *ACS Catal.*, 2024, **14**, 7289–7298.
59 X.-M. Hu, M. H. Rønne, S. U. Pedersen, T. Skrydstrup and K. Daasbjerg, *Angew. Chem., Int. Ed.*, 2017, **56**, 6468–6472.
60 A. N. Marianov, A. S. Kochubei, T. Roman, O. J. Conquest, C. Stampfl and Y. Jiang, *ACS Catal.*, 2021, **11**, 3715–3729.
61 Z. Wang, B. Mei, Y. Xu, Y. Liu, X. Li and R. Cao, *ChemCatChem*, 2025, **17**, e202402090.
62 S. Aoi, K. Mase, K. Ohkubo and S. Fukuzumi, *Chem. Commun.*, 2015, **51**, 10226–10228.
63 E. Fujita, D. J. Szalda, C. Creutz and N. Sutin, *J. Am. Chem. Soc.*, 1988, **110**, 4870–4871.
64 E. Fujita, L. R. Furenlid and M. W. Renner, *J. Am. Chem. Soc.*, 1997, **119**, 4549–4550.
65 E. Fujita and R. van Eldik, *Inorg. Chem.*, 1998, **37**, 360–362.
66 J. Shen, R. Kortlever, R. Kas, Y. Y. Birdja, O. Diaz-Morales, Y. Kwon, I. Ledezma-Yanez, K. J. P. Schouten, G. Mul and M. T. M. Koper, *Nat. Commun.*, 2015, **6**, 8177.
67 Y. Y. Birdja, J. Shen and M. T. M. Koper, *Catal. Today*, 2017, **288**, 37–47.
68 Y. Y. Birdja, R. E. Vos, T. A. Wezendonk, L. Jiang, F. Kapteijn and M. T. M. Koper, *ACS Catal.*, 2018, **8**, 4420–4428.
69 A. J. Göttle and M. T. M. Koper, *J. Am. Chem. Soc.*, 2018, **140**, 4826–4834.
70 Q. Feng, Y. Sun, X. Gu and Z. Dong, *Electrocatalysis*, 2022, **13**, 675–690.
71 C. M. Lieber and N. S. Lewis, *J. Am. Chem. Soc.*, 1984, **106**, 5033–5034.
72 T. V. Magdesieva, T. Yamamoto, D. A. Tryk and A. Fujishima, *J. Electrochem. Soc.*, 2002, **149**, D89.
73 A. De Riccardis, M. Lee, R. V. Kazantsev, A. J. Garza, G. Zeng, D. M. Larson, E. L. Clark, P. Lobaccaro, P. W. W. Burroughs, E. Bloise, J. W. Ager, A. T. Bell, M. Head-Gordon, G. Mele and F. M. Toma, *ACS Appl. Mater. Interfaces*, 2020, **12**, 5251–5258.
74 X. Zhang, Z. Wu, X. Zhang, L. Li, Y. Li, H. Xu, X. Li, X. Yu, Z. Zhang, Y. Liang and H. Wang, *Nat. Commun.*, 2017, **8**, 14675.
75 Z. Jiang, Y. Wang, X. Zhang, H. Zheng, X. Wang and Y. Liang, *Nano Res.*, 2019, **12**, 2330–2334.
76 P. Tian, B. Zhang, J. Chen, J. Zhang, L. Huang, R. Ye, B. Bao and M. Zhu, *Catal. Sci. Technol.*, 2021, **11**, 2491–2496.
77 J.-J. Ma, H.-L. Zhu, Y.-Q. Zheng and M. Shui, *ACS Appl. Energy Mater.*, 2021, **4**, 1442–1448.
78 M. Huai, Z. Yin, F. Wei, G. Wang, L. Xiao, J. Lu and L. Zhuang, *Chem. Phys. Lett.*, 2020, **754**, 137655.
79 M. Zhu, R. Ye, K. Jin, N. Lazouski and K. Manthiram, *ACS Energy Lett.*, 2018, **3**, 1381–1386.
80 S. Kapusta and N. Hackerman, *J. Electrochem. Soc.*, 1984, **131**, 1511.
81 C. L. Rooney, M. Lyons, Y. Wu, G. Hu, M. Wang, C. Choi, Y. Gao, C.-W. Chang, G. W. Brudvig, Z. Feng and H. Wang, *Angew. Chem., Int. Ed.*, 2024, **63**, e202310623.
82 A. Maurin and M. Robert, *J. Am. Chem. Soc.*, 2016, **138**, 2492–2495.
83 C. Zhang, D. Dragoe, F. Brisset, B. Boitrel, B. Lassalle-Kaiser, W. Leibl, Z. Halime and A. Aukauloo, *Green Chem.*, 2021, **23**, 8979–8987.
84 H. He, Y. Jian, J. Liu, Z. Yin, Q. Lu, H. Lei, W. Zhang and R. Cao, *ChemSusChem*, 2025, **18**, e202501485.
85 A. Tatin, C. Comminges, B. Kokoh, C. Costentin, M. Robert and J.-M. Savéant, *Proc. Natl. Acad. Sci. U. S. A.*, 2016, **113**, 5526–5529.
86 C. Zhang, J. Follana-Berná, D. Dragoe, Z. Halime, P. Gotico, Á. Sastre-Santos and A. Aukauloo, *Angew. Chem., Int. Ed.*, 2024, **63**, e202411967.
87 J. Choi, J. Kim, P. Wagner, S. Gambhir, R. Jalili, S. Byun, S. Sayyar, Y. M. Lee, D. R. MacFarlane, G. G. Wallace and D. L. Officer, *Energy Environ. Sci.*, 2019, **12**, 747–755.
88 T. Burdyny and W. A. Smith, *Energy Environ. Sci.*, 2019, **12**, 1442–1453.
89 L. Yao, K. E. Rivera-Cruz, N. Singh and C. C. McCrory, *Curr. Opin. Electrochem.*, 2023, **41**, 101362.
90 S. Ren, D. Joulié, D. Salvatore, K. Torbensen, M. Wang, M. Robert and C. P. Berlinguette, *Science*, 2019, **365**, 367–369.
91 F. Li, Y. C. Li, Z. Wang, J. Li, D.-H. Nam, Y. Lum, M. Luo, X. Wang, A. Ozden and S.-F. Hung, *Nat. Catal.*, 2020, **3**, 75–82.
92 J. Su, J.-J. Zhang, J. Chen, Y. Song, L. Huang, M. Zhu, B. I. Yakobson, B. Z. Tang and R. Ye, *Energy Environ. Sci.*, 2021, **14**, 483–492.
93 H. Li, Y. Pan, Z. Wang, Y. Yu, J. Xiong, H. Du, J. Lai, L. Wang and S. Feng, *Nano Res.*, 2022, **15**, 3056–3064.
94 D. Wakerley, S. Lamaison, J. Wicks, A. Clemens, J. Feaster, D. Corral, S. A. Jaffer, A. Sarkar, M. Fontecave and E. B. Duoss, *Nat. Energy*, 2022, **7**, 130–143.
95 F. Habibzadeh, P. Mardle, N. Zhao, H. D. Riley, D. A. Salvatore, C. P. Berlinguette, S. Holdcroft and Z. Shi, *Electrochem. Energy Rev.*, 2023, **6**, 26.

96 M. Heßelmann, H. Minten, T. Geissler, R. G. Keller, A. Bardow and M. Wessling, *Adv. Sustainable Syst.*, 2023, **7**, 2300077.
97 J. Yu, J. Xiao, Y. Ma, J. Zhou, P. Lu, K. Wang, Y. Yan, J. Zeng, Y. Wang, S. Song and Z. Fan, *Chem Catal.*, 2023, **3**, 100670.
98 S. Garg, C. A. G. Rodriguez, T. E. Rufford, J. R. Varcoe and B. Seger, *Energy Environ. Sci.*, 2022, **15**, 4440–4469.
99 Q. Xu, S. Liu, F. Longhin, G. Kastlunger, I. Chorkendorff and B. Seger, *Adv. Mater.*, 2024, **36**, 2306741.
100 M. Wang, A. Loiudice, V. Okatenko, I. D. Sharp and R. Buonsanti, *Chem. Sci.*, 2023, **14**, 1097–1104.
101 M. Abdinejad, A. Farzi, R. Möller-Gulland, F. Mulder, C. Liu, J. Shao, J. Biemolt, M. Robert, A. Seifitokaldani and T. Burdyny, *Nat. Catal.*, 2024, **7**, 1109–1119.
102 B. Kumar, B. Muchharla, M. Dikshit, S. Dongare, K. Kumar, B. Gurkan and J. M. Spurgeon, *Environ. Sci. Technol. Lett.*, 2024, **11**, 1161–1174.
103 D. Segets, C. Andronescu and U.-P. Apfel, *Nat. Commun.*, 2023, **14**, 7950.
104 C. P. O'Brien, R. K. Miao, A. Shayesteh Zeraati, G. Lee, E. H. Sargent and D. Sinton, *Chem. Rev.*, 2024, **124**, 3648–3693.
105 Y. Segura-Ramirez, M. Gomez-Mingot, M. Fontecave and C. M. Sánchez-Sánchez, *ChemSusChem*, 2025, **18**, e202500392.
106 B. Mondal, P. Sen, A. Rana, D. Saha, P. Das and A. Dey, *ACS Catal.*, 2019, **9**, 3895–3899.
107 X. Lu, Z. Jiang, X. Yuan, Y. Wu, R. Malpass-Evans, Y. Zhong, Y. Liang, N. B. McKeown and H. Wang, *Sci. Bull.*, 2019, **64**, 1890–1895.
108 B. Belsa, L. Xia and F. P. García de Arquer, *ACS Energy Lett.*, 2024, **9**, 4293–4305.
109 H. Shin, K. U. Hansen and F. Jiao, *Nat Sustainability*, 2021, **4**, 911–919.
110 M. Bernt, A. Hartig-Weiß, M. F. Tovini, H. A. El-Sayed, C. Schramm, J. Schröter, C. Gebauer and H. A. Gasteiger, *Chem. Ing. Tech.*, 2020, **92**, 31–39.
111 L. Que Jr, *JBIC, J. Biol. Inorg. Chem.*, 2006, **11**, 1.
112 K. D. Koehntop, S. Marimanikkuppam, M. J. Ryle, R. P. Hausinger and L. Que Jr, *JBIC, J. Biol. Inorg. Chem.*, 2006, **11**, 63–72.
113 https://www.siemens-energy.com/global/en/home/press-releases/research-project-rheticus.html.
114 A. Smith, Z. Halime, C. Herrero and A. Aukauloo, *ChemCatChem*, 2025, e01217.
115 J. A. Laureanti, M. O'Hagan and W. J. Shaw, *Sustain. Energy Fuels*, 2019, **3**, 3260–3278.
116 Z. Yin, M. Zhang, Y. Long, H. Lei, X. Li, X.-P. Zhang, W. Zhang, U.-P. Apfel and R. Cao, *Angew. Chem., Int. Ed.*, 2025, **64**, e202500154.